On-orbit vicarious calibration of ocean color sensors using an ocean surface reflectance model

P. Jeremy Werdell,[1,*] Sean W. Bailey,[1] Bryan A. Franz,[1] André Morel,[2] and Charles R. McClain[1]

[1]NASA Goddard Space Flight Center, 614.2, Greenbelt, Maryland 20771, USA
[2]Laboratoire d'Océanographie de Villefranche, Université Pierre et Marie Curie and Centre National de la Recherche Scientifique, Villefranche-sur-Mer, France

*Corresponding author: paul.j.werdell@nasa.gov

Received 8 March 2007; revised 18 May 2007; accepted 22 May 2007;
posted 23 May 2007 (Doc. ID 80628); published 8 August 2007

Recent advances in global biogeochemical research demonstrate a critical need for long-term ocean color satellite data records of consistent high quality. To achieve that quality, spaceborne instruments require on-orbit vicarious calibration, where the integrated instrument and atmospheric correction system is adjusted using *in situ* normalized water-leaving radiances, such as those collected by the marine optical buoy (MOBY). Unfortunately, well-characterized time-series of *in situ* data are scarce for many historical satellite missions, in particular, the NASA coastal zone color scanner (CZCS) and the ocean color and temperature scanner (OCTS). Ocean surface reflectance models (ORMs) accurately reproduce spectra observed in clear marine waters, using only chlorophyll *a* (C_a) as input, a measurement for which long-term *in situ* time series exist. Before recalibrating CZCS and OCTS using modeled radiances, however, we evaluate the approach with the Sea-viewing Wide-Field-of-view Sensor (SeaWiFS). Using annual C_a climatologies as input into an ORM, we derive SeaWiFS vicarious gains that differ from the operational MOBY gains by less than $\pm 0.9\%$ spectrally. In the context of generating decadal C_a climate data records, we quantify the downstream effects of using these modeled gains by generating satellite-to-*in situ* data product validation statistics for comparison with the operational SeaWiFS results. Finally, we apply these methods to the CZCS and OCTS ocean color time series.

OCIS codes: 010.4450, 280.0280, 120.0280, 030.5620.

1. Introduction

The marine biosphere contributes significantly to processes that regulate the Earth's climate. Ocean color satellites provide the scientific community a means of studying the biosphere on temporal and spatial scales unattainable using conventional *in situ* sampling platforms, such as research vessels, drifters, or permanent moorings. The NASA Sea-viewing Wide Field-of-view Sensor (SeaWiFS) has been producing a continuous, global marine bio-optical data set since late 1997. SeaWiFS measures the spectra of reflected sunlight emanating upward from the top of the Earth's atmosphere at six visible and two near-infrared wavebands. Spectral water-leaving radiances, $L_w(\lambda)$, the light backscattered out of the ocean, are obtained by removing the contribution of the atmosphere from the total signal [1]. The $L_w(\lambda)$ are subsequently used to estimate a number of geophysical data parameters through the application of secondary bio-optical algorithms [2]. The community relies heavily on SeaWiFS data products, the concentration of the phytoplankton pigment chlorophyll *a* (C_a), in particular, to support studies ranging from management of regional ecosystems to the development of decadal climate records [3].

Bailey and Werdell [4] recently demonstrated that SeaWiFS $L_w(\lambda)$ approach their assigned prelaunch goal of 5% absolute accuracy. This radiometric quality results, in part, from the mission-long on-orbit vicarious calibration [5–7] executed by the NASA Ocean Biology Processing Group (OBPG) to refine the integrated instrument-atmospheric correction system. After temporal changes in sensor responsitivity are characterized using lunar and solar diffuser ob-

0003-6935/07/235649-18$15.00/0

servations [8], SeaWiFS visible radiances are adjusted to force agreement with the normalized water-leaving radiances, $L_{wn}(\lambda)$, from the marine optical buoy [9] (MOBY), deployed 15 km west of Lanai, Hawaii. The terms from the vicarious calibration are given as fractional gain factors $\bar{g}(\lambda)$, with values of unity indicating no correction. During data processing, these gain factors are applied at the top-of-the-atmosphere, effectively updating the prelaunch sensor calibration, and thereby accounting for undetermined postlaunch changes to the instrument (resulting from, for example, orbit-raising maneuvers).

NASA has acquired well-calibrated, hyperspectral data from MOBY near-continuously since mid-1997 (a preoperational deployment of MOBY occurred from November 1996 to February 1997). Unfortunately, similar time series of *in situ* radiometric data do not exist during the eras of the SeaWiFS predecessors, in particular, the NASA coastal zone color scanner (CZCS) and the National Space Development Agency of Japan (NASDA; now known as the Japan Aerospace Exploration Agency) ocean color and temperature scanner (OCTS). Ocean surface reflectance models (ORMs) developed for the visible part of the spectrum have been shown to reproduce accurately the radiance spectra observed in the field, at least for deep marine waters [10,11]. These models generally permit the estimation of plausible, average $L_{wn}(\lambda)$ using a single input parameter, C_a, which is used as a proxy for the bulk bio-optical properties of oceanic Case-1 [12] waters. Given that long-term and seasonal time series of *in situ* C_a exist [13], we propose that continuous, regional time series of C_a in combination with an ORM provide a viable data source for the vicarious calibration of ocean color satellites in the absence of abundant *in situ* radiometry. Such a concept is not novel *per se*, as Evans and Gordon [14] successfully used fixed, theoretical clear-water radiances to calibrate the CZCS bands at 520 and 550 nm.

Here, we relax the constraint of fixed radiances and evaluate the utility of an ORM allowed to vary temporally with C_a for the visible-band vicarious calibration of SeaWiFS. Our multistep approach begins with a description of the C_a-driven ORM developed by Morel and Maritorena [11] (MM01) for Case-1 waters. We then acquire and evaluate regional C_a time series from the well-established U.S. Joint Global Ocean Flux Study (JGOFS) Bermuda Atlantic Time series Study (BATS) and Hawaiian Ocean Time series (HOT) hydrostations. These C_a are used in combination with the ORM to build a regional time series of modeled $L_{wn}(\lambda)$ for the Sargasso Sea and North Pacific Subtropical Gyre (NPSG). The radiances are used in turn to derive independent $\bar{g}(\lambda)$ for SeaWiFS, which are subsequently compared to the operational vicarious gains derived from MOBY radiometry. Finally, we quantify the downstream effect of using the model-based vicarious gains by incorporating them into the OBPG satellite-to-*in situ* data product validation system for comparison with the operational SeaWiFS results [4]. After vetting the approach with SeaWiFS, we apply the methods to the historical CZCS and OCTS ocean color time series, with the intent of developing an updated baseline technique for their retrospective visible-band calibration.

2. Modeling Approach

A. Model Development

Spectral subsurface irradiance reflectance (the ratio of upward to downward irradiance), $R(0^-)$ has been related to the ratio $X = b_b/(a + b_b)$ through a polynomial [15] expression, where a and b_b are the total absorption and backscattering coefficients, respectively. In this expansion, the first term is predominant such that the polynomial can be reduced to:

$$R(0^-) = f' \frac{b_b}{a + b_b}, \tag{1}$$

provided that appropriate values of the dimensionless term f' have been produced. This term varies with the composition of the water body, the illumination (Sun + sky) conditions, and the sea state. Spectral dependencies are omitted for brevity unless required for clarity. Using Eq. (1), we estimate L_{wn} via:

$$L_{wn} = \Re F_0 \frac{R(0^-)}{Q}, \tag{2}$$

where F_0 is the mean extraterrestrial solar irradiance, Q is the ratio of the upwelling irradiance to the upwelling radiance at nadir (equal to π for a totally diffuse radiance distribution), and $\Re$ describes the combined reflection and refraction effects that occur as downward irradiance and upward radiance propagate through the air-sea interface [10,16,17].

For simplicity, we adopt a constant value of $\Re = 0.529$, which is valid when the solar zenith angle and wind speed are not too large [17]. The remaining unknowns in Eqs. (1) and (2) include only a, b_b, f', and Q. Conveniently, Morel *et al.* [16] describe both f' and Q spectrally as a function of C_a and solar zenith angle θ_0, using a series of lookup tables (LUT; available at http://www.obs-vlfr.fr/~morel). We refer the reader to Morel and Mueller [18] for a detailed review of f' and Q and their role in the remote sensing paradigm. The estimation of both a and b_b from C_a, however, warrants additional description, as these relationships are likely candidates for update in subsequent analyses.

In seawater, the backscattering coefficient can be partitioned into its water and particulate components using $b_b = b_{bw} + b_{bp}$, where the subscripts w and p indicate water and particles, respectively, and the former is considered known. The particulate backscattering spectrum is described by $b_{bp} = \tilde{b}_{bp} \times b_p$, where $\tilde{b}_{bp}$ is the particulate backscattering ratio (the ratio of backscattering to total scattering) and b_p is the particulate scattering spectrum. *In situ* measurements of b_p have been empirically related [19] to C_a using

$$b_p\,(550) = BC_a^E. \tag{3}$$

MM01 most recently described this relationship using 0.416 and 0.766 for B and E, respectively. The validity of Eq. (3) for BATS and HOT will be reviewed in Subsection 2.B.

The spectral dependency of light scattering is primarily a function of the particle size distribution, which is reviewed in detail elsewhere [20] and often described via λ^{v}. MM01 adopted a C_a-controlled spectral variation that maintains a λ^{-1} dependency at $C_a < 0.02$ mg m^{-3}, where small detrital particles are optically dominant, and serially diminishes to λ^0 at $C_a \geq 2$ mg m^{-3} [their Eq. (14)]. With the $\tilde{b}_{bp}$ introduced in Eq. (13) of MM01, the spectral particulate backscattering coefficient is fully expressed as

$$b_{bp}(\lambda) = \{0.002 + 0.01[0.5 - 0.25 \log_{10} C_a]\} \times b_p\,(550)\left(\frac{\lambda}{550}\right)^{v}, \tag{4}$$

where λ is wavelength, 550 nm is a nominal scaling wavelength from Eq. (3), and the expression in braces describes $\tilde{b}_{bp}$. In Eq. (4), the constant background term (set to 0.002) and decimal logarithm of C_a (in brackets) describe a maximal backscattering efficiency of 1.2% at 550 nm when $C_a = 0.01$ mg m^{-3}. If we temporarily adopt bounding C_a values of 0.05 and 0.25 mg m^{-3} for our study sites of BATS and HOT (Figs. 1 and 2), Eq. (4) produces $\tilde{b}_{bp}(550)$ of 0.0103 and 0.0085, respectively, which is consistent with recent *in situ* observations collected in different environments [21–23].

Considering the same bounding C_a values, we estimate v of -0.8 and -0.45, respectively, using Eq. (13) of MM01. By design, these are typical of assemblages of larger phytoplankton [24] (>2 μm), but not of smaller particles (0.2–0.5 μm), such as viruses, bacteria, and small eukaryotic algal cells, which have values closer to -2 and are now thought to make the dominant contribution to b_{bp} in oligotrophic waters [25]. Bacterial assemblages have been shown to dominate the waters around both BATS and HOT [26,27]. As such, we replace the MM01 v with the parameterization of Ciotti *et al.* [28] (their Eq. (24)):

$$v = 1 - 0.768 \log_{10} C_a, \tag{5}$$

which assumes that the scattering spectral dependency follows λ^{-2} when $C_a \sim 0.05$ mg m^{-3} and λ^0 when $C_a \sim 20$ mg m^{-3}. Using Eq. (5), the same bounding C_a produce v values of -2 and -1.46. For comparison, Loisel *et al.* [29] inverted SeaWiFS radiometry to derive mean annual v values of ~ -1.5 and ~ -2 for the BATS and HOT regions, respectively (see their Fig. 3), and a mean annual average of -1.37 (± 0.42 standard deviation). The net effect of replacing the MM01 v with Eq. (5) is a radiometric brightening that increases with decreasing wavelength, which will be supported by *in situ* observations we describe in Subsection 2.B.

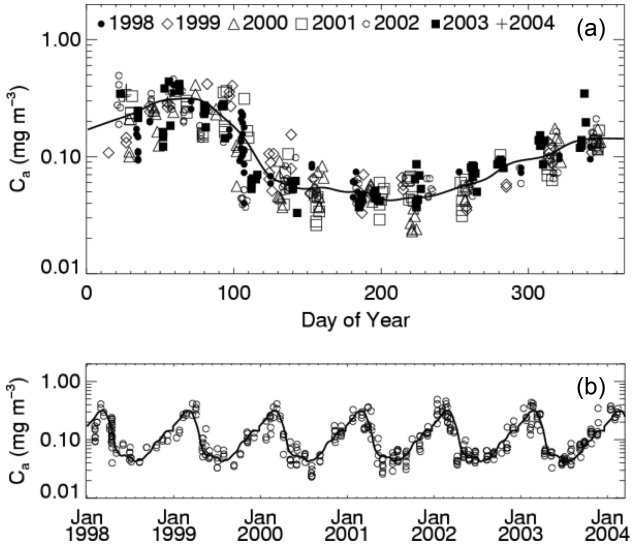

Fig. 1. Near-surface C_a measurements from the BATS site for years 1998–2004 (symbols) and a smoothed fit to these data (solid line). To generate this fit, we first organized the C_a by day of year and then sorted them into biweekly bins (resulting in 26 sequential 14-day collections). We then calculated the mean of the semi-interquartile range for each bin, and smoothed this mean time-series by recalculating the three-element central moving-average for each bin. Several undersampled bins whose means proved to be outliers precipitated the latter time-series filter. Finally, we redisplayed the means temporally using the central day number for each bin, and used cubic spline interpolation to estimate C_a for every day of the year (roots of residual mean squares of 0.066 and 0.010 for BATS and HOT, respectively). Data are displayed as a function of day of year (a) and a multiannual time-series (b). Using the generalized fit, C_a may be estimated from the day of year. The sample sizes are 45, 41, 43, 54, 64, 58, and 9 for 1998 through 2004, respectively.

Significant uncertainty resides in both the empirical and analytical components of Eqs. (3)–(5), but global data sets for independent verification are uncommon. Alternative formulations exist [21–23], yet debates over the backscattering properties of oceanic particles and field instrumentation persist [20]. In Case-1 waters, the temporally and spatially varying relative concentrations of algae and other particulates, or variations within the plankton assemblages, almost certainly modify the C_a-to-b_b relationship [24], particularly with varying particle size distributions [25]. Without *a priori* knowledge of such dynamics, however, the use of Eqs. (3)–(5) provides a moderately accurate and convenient expression of b_b for the C_a-driven ORM.

The absorption coefficient of seawater is also commonly partitioned into components using $a = a_w + a_\phi + a_{n\phi} + a_g$, where the subscripts w, ϕ, $n\phi$, and g indicate water, phytoplankton, nonphytoplankton particles, and dissolved organics, respectively, and a_w is considered known. While the relationship between C_a and a_ϕ has been extensively studied [30], as has that between C_a and total particulate absorption

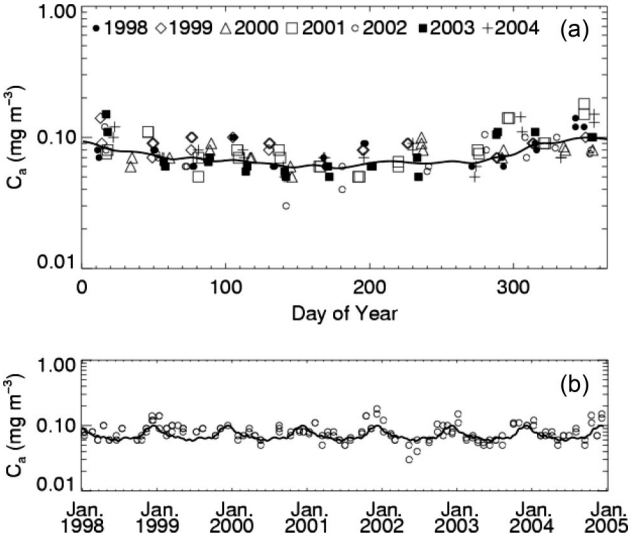

Fig. 2. Near-surface C_a measurements from the HOT site for years 1998–2004 (symbols) and a smoothed fit to these data (solid line; see the caption of Fig. 1 for details). Data are displayed as a function of day of year (a) and a multiannual time-series (b). Using the generalized fit, C_a may be estimated from the day of year. The sample sizes are 24, 22, 19, 21, 19, 20, and 22 for 1998 through 2004, respectively.

($= a_\phi + a_{n\phi}$) in Case-1 conditions [31], the global correlation between C_a and a_g is weak [32]. A C_a-based relationship for $a_g(440)$, using $a_\phi(440)$, has been proposed [33], but remains unverified. Further, the determination of $a_g(\lambda)$ requires independent knowledge of its spectral slope [34], a parameter that varies significantly [35] and does not appear to be related to C_a.

In contrast, the spectral diffuse downwelling attenuation coefficient K_d encompasses the effects of all absorbing material in the water column, including that of dissolved organics, and is used routinely in lieu of a in ORM applications [10,11]. MM01 revisited the correlation between C_a and the biological component of K_d:

$$K_d = \chi C_a^e + K_w, \tag{6}$$

where spectral χ and e are provided in MM01 Table 2 and K_w is the term for pure water. The validity of Eq. (6) for BATS and HOT will be reviewed in Subsection 2.B. Using numerical simulations, Gordon [36] related K_d to the absorption and backscattering coefficients through $K_d = 1.0395(\mu_d)^{-1}(a + b_b)$, where μ_d is the average cosine of the downward flux below the surface. As for f' and Q, Morel and Gentili [37] describe μ_d spectrally as a function of C_a and θ_0 using a LUT. When solved for a using Eq. (1), the relationship becomes

$$a = 0.962K_d\mu_d\left(1 - \frac{R(0^-)}{f'}\right). \tag{7}$$

Note that as $R(0^-)$ is a small number, K_d remains the principal property in Eq. (7).

The goal of the present approach is to produce $R(0^-)$ as a function of C_a using estimates of b_b and a (using Eqs. (4) and (7), respectively) as input into Eq. (1). As in MM01, we require an iterative approach, as $R(0^-)$ (the unknown) appears in Eq. (7). First, both f' and μ_d are estimated using LUTs as described above. By calculating b_{bp} and K_d using Eqs. (4) and (6), respectively, and making an initial guess at a using $[0.962K_d\ \mu_d]$, we derive a first set of $R(0^-)$ values through Eq. (1). These values are used to adjust a using Eq. (7), which are subsequently used to derive more accurate $R(0^-)$ through a second loop. Stable a values, and therefore $R(0^-)$ values, are obtained within three loops of this iterative process. Finally, spectral Q are estimated using a LUT as described above, and L_{wn} are calculated using Eq. (2). Note that we do not explicitly account for Raman or inelastic scattering in this formulation, despite the need to calculate a SeaWiFS vicarious gain at 670 nm.

A final radiometric normalization is required to accurately compare L_{wn} collected under varied geometric conditions, as is our need in the vicarious calibration process [18]. An anisotropic light field influences L_{wn} retrieved under different viewing and solar geometries, as affected by local illumination conditions and resident concentrations of in-water constituents (and their scattering properties). In practice, we "exactly" normalize L_{wn} to the case of sensor and solar zenith angles = 0° using a geometry- and C_a-based LUT (similar to those described previously), where C_a acts as a proxy for all of the bio-optical components [16]. For simplicity, in our initial derivation of L_{wn}, we use a constant solar zenith angle of 30°. This is consistent with applications and discussions presented in MM01 and Morel and Gentili [37], and with the experimental conditions under which the data used to derive the above empirical relationships were collected (predominantly $15° \le \theta_0 \le 45°$). Our final step is the calculation of "exact" L_{wn} (from $\theta_0 = 30°$ to $\theta_0 = 0°$). The ultimate radiometric product is spectral L_{wn} derived using only C_a as input.

B. Model Validation

Before proceeding, we verified the ability of the ORM to replicate observed radiances through a comparison of modeled remote-sensing reflectance R_{rs} (the ratio of water-leaving radiance to surface irradiance; alternatively calculated using L_{wn}/F_0), with *in situ* measurements collected at the BATS and HOT sites. We also evaluated the C_a-based expressions for K_d, b_p, and Q used within the ORM. Observations of C_a and spectral radiometry at both sites were acquired from the NASA SeaWiFS Bio-optical Archive and Storage System (SeaBASS) [38]. Spectral R_{rs} and K_d were derived from the radiometric profiles following Werdell and Bailey [39]. Beam attenuation measurements at 660 nm at both sites were acquired from the Texas A&M University transmissometer database [40]. Average surface values were calculated for each

transmissometer profile (using all data collected <10 m; maximum standard deviations of 0.06 and 0.02 m^{-1} for BATS and HOT, respectively). Globally distributed measurements of Q (from profiles of upwelling irradiance and upwelling nadir radiance) were acquired from the NASA Self Consistent AOP Profile Archive (SCAPA) [41]. Here, spectral Q were calculated as the average ratio of upwelling irradiance to the upwelling radiance collected just below the sea surface. All data were paired with a coincident C_a value, when available.

To review the spectral shape of the modeled radiometry, we first stratified the *in situ* data into limited ranges of C_a centered on 0.05 and 0.25 mg m^{-3} for BATS and 0.08 mg m^{-3} for HOT (Figs. 1 and 2). *In situ* stations within ±33% of each typical C_a were identified, and coincident observations of R_{rs} were averaged. This mean radiometry was compared with the modeled R_{rs} calculated for each typical C_a (Fig. 3). Such an analysis permits the simultaneous verification of both the shape and magnitude of the modeled spectra without overemphasizing variability associated with the field observations themselves (as would be the case for scatter plots). The ORM visually reproduces the spectral shape of the field observations for all cases, but maintains a slight tendency to be spectrally flat relative to the *in situ* data (e.g., slightly high at 555 nm for BATS with C_a = 0.25 mg m^{-3} and slightly low at 412 nm for HOT with C_a = 0.08 mg m^{-3}). It is worth recalling that the magnitude and shape of this bias would increase were the MM01 v not replaced by Eq. (5). Modeled values >600 nm are higher than observed *in situ* for all cases.

The predominant source of this bias is not immediately apparent, even when individual components of the ORM are regionally evaluated. This is mainly because of the paucity of relevant *in situ* data sets that would permit empirical analyses of certain model components, for example, f'. Those measurements that are currently available, however, merit some discussion. With regard to Q, using data from nine stations in the Gulf of California, Voss and Morel [42] found the adopted parameterization to replicate *in situ* measurements to within 7%. On average, the SCAPA data support this conclusion for the range $0.05 \le C_a \le 0.25$ mg m^{-3}, reporting differences of $-3.8 \pm 15\%$ and $6.4 \pm 16\%$ for nadir $Q(443)$ and $Q(555)$, respectively, and no discernible variation over the dynamic range of C_a. Despite this, a regional examination of SCAPA shows the model Q to differ significantly on a station-by-station basis (up to ±20%, as partially indicated by the standard deviations reported above). Uncertainties in Q propagate into derived L_{wn} directly through Eq. (1) and, to a lesser degree, through its "exact" normalization [16]. Note that modifying Q by the average SCAPA percent differences listed above shifts the derived spectra in a desirable direction, by raising $L_{wn}(443)$ and lowering $L_{wn}(555)$. Unfortunately, to our knowledge, Q is currently not collected at the BATS and HOT sites.

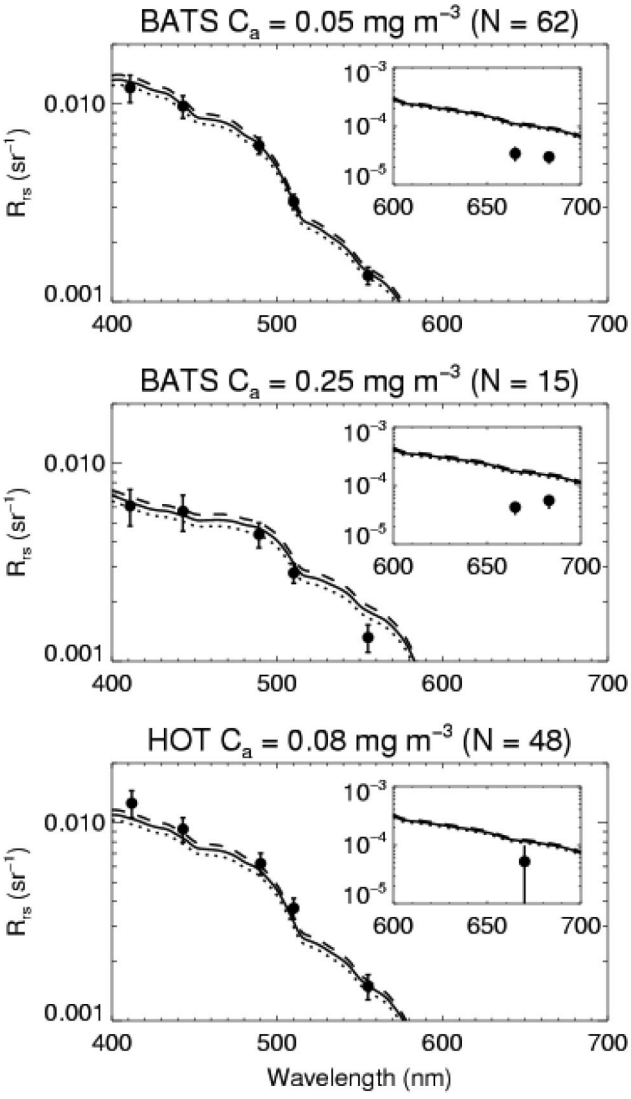

Fig. 3. Validation of the ORM using *in situ* measurements collected at the BATS and HOT sites. *In situ* stations with a given C_a level were identified (± an appropriate threshold value) and corresponding "exact" R_{rs} were averaged (solid circles) for comparison with the ORM output for $\theta_0 = 15°$ (dotted line), 30° (solid line), and 45° (dashed line). *In situ* standard deviations are shown as vertical bars. Sample sizes in figure titles.

With regards to K_d, Eq. (6) fairly accurately reproduces the distribution of observations made at BATS, albeit 5.4% high on average [Fig. 4(a)]. The C_a-to-K_d relationship shows almost no dynamic range for HOT, and Eq. (6) overestimates the *in situ* observations by 20.5% on average [Fig. 4(b)]. Naturally, in Eq. (1), artificially high K_d (and, therefore, a) diminish the magnitude of the modeled radiances. Sensitivity analyses indicate that overestimation of K_d by 5% and 20% lead to underestimation of R_{rs} by 4.8% and 16.8%, respectively, at C_a = 0.1 mg m^{-3}. Although not significant at BATS, the elevated K_d at HOT certainly contributed to the reduced radiances output by the ORM. Unfortunately, the paucity of hyperspectral *in situ* radiometry and limited dynamic range prohibit robust regional reconstruction

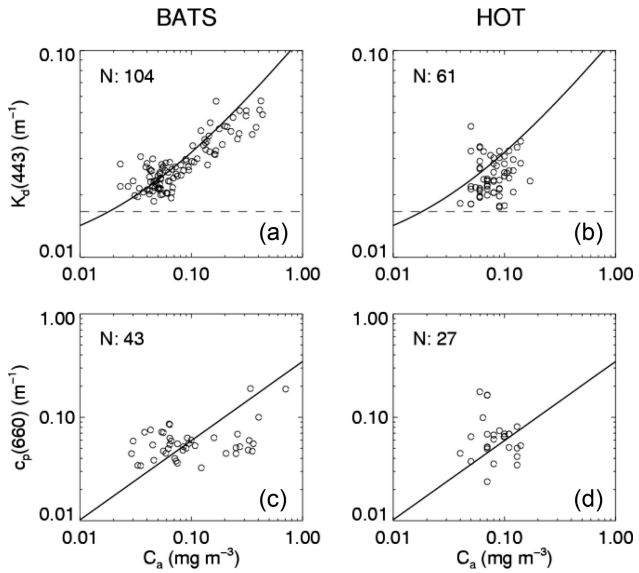

Fig. 4. Comparison of model estimates (solid lines) with *in situ* measurements (open circles) for $K_d(443)$ (per Eq. (6)) and $c_p(660)$ (per Eq. (6) of Loisel and Morel [19]). Results for $K_d(443)$ are presented in panels (a) and (b), where the horizontal dashed lines demark the pure seawater value, and results for $c_p(660)$ are presented in panels (c) and (d). Results for BATS are presented in panels (a) and (c), and for HOT in (b) and (d).

of Eq. (6) at either site. Seemingly, this narrow radiometric dynamic range persists in most low C_a waters (see, e.g., Fig. 9 of Werdell and Bailey [39]), reinforcing the need for biogeographically rich data sets to derive statistical relationships such as Eq. (6).

The C_a-to-b_p relationship described in Eq. (3) was derived using beam attenuation data collected at 660 nm. This is effectively a measurement of particle scattering, as attenuation by dissolved material at that wavelength is negligible in marine environments. Once the contribution of pure seawater is removed from the total attenuation coefficient (0.364 m^{-1}), the remaining value is referred to as the particulate beam attenuation coefficient, $c_p(660)$, which is approximately equal [19] to $b_p(660)$. In Figs. 4(c) and 4(d) we compare coincident C_a and $c_p(660)$ measurements with the Eq. (6) of Loisel and Morel [19], which was adopted by MM01 to derive Eq. (3) via a λ^{-1} scattering spectral dependency to migrate the scaling wavelength from 660 to 550 nm. While significant scatter exists for both the BATS and HOT sites, the overall magnitude of the modeled $c_p(660)$ appears to be in line with the *in situ* observations (i.e., no reported biases). Note, however, that for both sites, $c_p(660)$ varies little with C_a, in agreement with that reported for these sites by Behrenfeld and Boss [43]. With a few exceptions, time-series of $c_p(660)$ (not shown) display little annual variation as well, at least for these limited data sets. While the dynamic range in C_a-to-$c_p(660)$ at BATS would permit a regional rederivation of Eq. (3) (unlike for HOT), sensitivity analyses suggest that little improvement in the ORM would be realized at this time.

3. C_a Climatology Development Validation

A. Site Selection

We next acquire and evaluate long-term C_a time-series to be used as input into the ORM. In 1988, the U.S. National Science Foundation established the US JGOFS BATS [44] and HOT [45] (Station ALOHA) stations to facilitate deep ocean physical and biogeochemical research. Each hydrostation is visited approximately monthly, resulting in well-studied, decadal time-series of C_a that capture the annual biogeophysical variability of the Sargasso Sea and NPSG. In 1992, routine measurement of *in situ* radiometry commenced in conjunction with the BATS observational program. Likewise, radiometric measurements were added to the standard HOT suite of observations in early 1998. Just after its launch in late 1997, SeaWiFS began collecting Local Area Coverage (LAC) data (~1 km^2 at nadir) over both hydrostations, which fortuitously precludes the use of the subsampled Global Area Coverage (GAC) data (~20 km^2 at nadir) in this calibration activity.

We make several simplifying assumptions about both the BATS and HOT sites to ensure their viable use as ocean color satellite calibration sites. First, in accordance with the calibration guidelines posed by Gordon [5], we assume that each area experiences (1) predominantly maritime aerosols with an optical thickness of approximately 0.1, and (2) spatially homogeneous $L_{wn}(\lambda)$ on a scale of several kilometers. The former was recently verified by Smirnov *et al.* [46], who report annual mean and mode aerosol optical thicknesses at 500 nm of 0.14 and 0.09 for Bermuda and 0.07 and 0.06 for Lanai, Hawaii. For the latter, although mesoscale eddies recur in the western Sargasso Sea [47], their sizes (100–150 km) significantly exceed that of the aggregated satellite observations (5–20 km) used in operational vicarious calibration [7]. The western Sargasso Sea remains otherwise relatively unperturbed on such small scales. Horizontal gradients are similarly weak within the NPSG [48].

Second, based on their considerable distance from terrigeneous influences, we assume that the BATS and HOT sites largely maintain Case-1 conditions, which is a prerequisite for an ORM that accepts C_a as its only input. The seasonal biogeochemical patterns at BATS and HOT have been analyzed [27,49]. In the Sargasso Sea, seasonal variation of colored dissolved materials, which are not directly correlated with the algal standing stock, have also been described [50]. As the development of the ORM rests on the use of average empirical relationships, specifically Eqs. (3) and (6), notable departures with respect to these averages will entail a partial failure in the predictive skill of the model. We acknowledge that such possible failures shape our conclusions.

B. Climatology Generation

We acquired 314 BATS and 147 HOT profiles of fluorometrically derived C_a from SeaBASS dating from

Table 1. SeaWiFS $\bar{g}$ and Standard Deviations[a] Calculated for MOBY and the ORM at the BATS and HOTS Sites

	N	412	443	490	510	555	670
MOBY	150 (42)	1.0377 (0.009)	1.0140 (0.009)	0.9927 (0.008)	0.9993 (0.009)	1.0002 (0.008)	0.9738 (0.007)
BATS	241 (45)	1.0345 (0.018)	1.0020 (0.016)	0.9814 (0.013)	0.9941 (0.011)	1.0016 (0.011)	0.9731 (0.006)
HOT	176 (45)	1.0300 (0.015)	1.0086 (0.012)	0.9879 (0.009)	0.9979 (0.008)	1.0046 (0.009)	0.9718 (0.006)
BATS + HOT	417 (90)	1.0323 (0.017)	1.0053 (0.015)	0.9847 (0.012)	0.9960 (0.010)	1.0031 (0.010)	0.9725 (0.006)

[a]In parentheses, with the exception of N, where we report the number of samples remaining after application of the semi-interquartile filter. Only these remaining samples are used to calculate the combined BATS + HOT $\bar{g}$_bar.

1998 to 2004. Near surface values were estimated following Werdell and Bailey [39]. The OBPG archive of MOBY data consists of ~225 days per year on average from 1998 to 2004. Given the relative small volume of BATS and HOT C_a data acquired in this time range, and the meager rate of return of suitable stations (i.e., number of matchups) in the vicarious calibration activity [7] (Table 1), we opted to generate a general climatological expression for these data to increase the sample size (Figs. 1 and 2; see captions for processing details). The annual shapes of the expressions agree well with that reported in Michaels *et al.* [49] for BATS and Ondrusek *et al.* [51] for HOT.

We verified these curves using C_a data from the NOAA National Oceanographic Data Center World Ocean Database 2005 [13] (WOD05). From the ocean station data subset of WOD05, we acquired 1578 fluorometric profiles of C_a collected near Bermuda dating from 1957 to 1998, and 367 profiles collected near Hawaii dating from 1982 to 1995. Regions were defined as 10° boxes centered on each hydrostation. The WOD05 C_a data were treated as described above and annual expressions were generated for both sites (Fig. 5). While minor discrepancies exist, the annual WOD05 expressions largely reproduce the curves generated using the SeaBASS data set.

The ocean color community largely considers high performance liquid chromatography (HPLC) to be the preferred method of retrieving C_a, as fluorometrically derived values are affected by the presence of accessory pigments. Variations in phytoplankton community structure change the accessory pigment content, and thus fluorometric inaccuracies vary seasonally and geographically [52]. While HPLC provides an advantage in this regard, Hooker *et al.* [53] report an average uncertainty of 17% for the retrieval of total C_a using HPLC. Ultimately, inaccuracies in C_a stem from the use of fluorometry in lieu of HPLC, uncertainties associated with both methods, and poor representation of actual conditions by the climatology. As such, we examined the sensitivity of the ORM output L_{wn} to its input C_a. If we vary C_a from a nominal value of 0.08 mg m^{-3} by +10% and −10%, the modeled L_{wn}(443) changes by −3.6% and +4.8%, respectively, and L_{wn}(555) changes by +1.3% and −1.4%, respectively. Similar results are obtained for C_a = 0.25 mg m^{-3}. A reduction in C_a shifts the radiometric spectra in a desirable direction, as reported in Subsection 2.B, by raising L_{wn}(443) and lowering L_{wn}(555).

Finally, we evaluated the combined ability of the model and C_a climatologies to reproduce seasonal

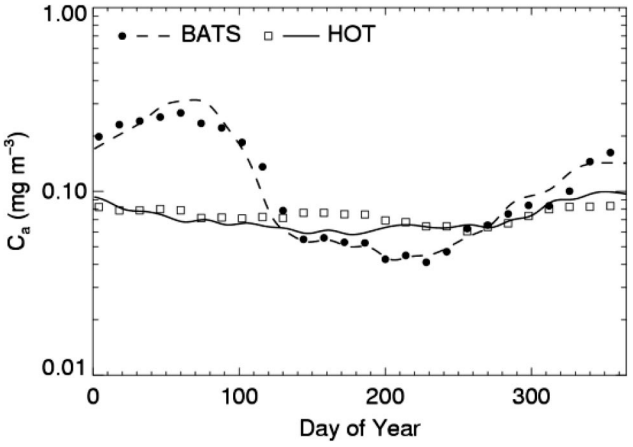

Fig. 5. Comparison of the generalized fits shown in Figs. 1 and 2 with similar curves generated using the NOAA WOD05 C_a data set for the BATS and HOT regions. The fits for Figs. 1 and 2 are redisplayed as dashed and solid lines for BATS and HOT, respectively. The WOD05 data are presented as solid circles and open squares for BATS and HOT, respectively.

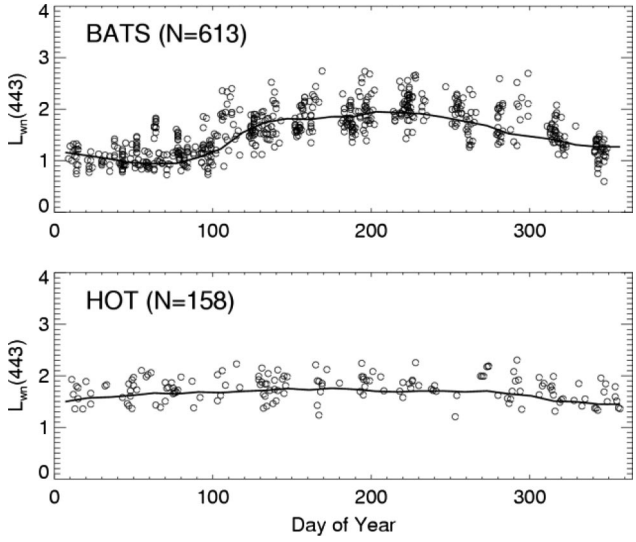

Fig. 6. Comparison of modeled L_{wn}(443) (solid lines) with *in situ* measurements (open circles) for the BATS (top) and HOT (bottom) sites. Here, C_a from the climatological expressions for C_a presented in Figs. 1 and 2 were used as input into the ORM. The L_{wn} units are μW cm^{-2} nm^{-1} sr^{-1}. Data are displayed as a function of the day of the year; 443 nm was highlighted given its predominance in C_a absorption spectra.

trends in observed BATS and HOT radiometry. To do so, we used the SeaBASS radiometric and pigment data that were originally presented in Subsection 2.A. The R_{rs} were organized by day of year and compared with the modeled R_{rs} calculated using the appropriate C_a climatology (Fig. 6). In particular, we highlight $R_{rs}(443)$ because of its predominance in C_a absorption spectra. Overall, the ORM-C_a climatology combination accurately reproduces the seasonal trends at both sites (residual mean squares of 0.058 and 0.0069 at 443 nm for BATS and HOT, respectively). At BATS, the low radiances in the winter (corresponding to the annual C_a bloom) and high radiances in the summer are both well represented in the modeled $R_{rs}(443)$. The tendency of the model to be subtly low relative to the *in situ* data, however, reappears in this analysis (biases of -0.093 and -0.110 at 443 nm for BATS and HOT, respectively). As for the previous analysis, the biases are spectrally dependent and diminish with increasing wavelength.

4. SeaWiFS Vicarious Calibration

We refer the reader to Franz *et al.* [7] for a complete discussion of the OBPG vicarious calibration approach. Before proceeding, however, a few points merit review. First, note that all temporal trends in sensor responsivity are removed *a priori* [8] and that the NIR vicarious calibration is completed prior to initiating the visible band calibration [7]. The ORM does not play a role in the NIR calibrations, as L_w is considered negligible in that process. Second, recall that we ultimately desire a single, temporally independent vicarious gain for each visible band to be applied during operational data processing. The evaluation of many calibration targets results in an accumulation of discrete gain factors g_i (one gain for each target i), from which an average vicarious gain $\bar{g}$ is calculated.

Using the annual expressions for C_a as input into the ORM, we calculated SeaWiFS-specific L_{wn} for every day of 1998 through mid-2006 at both the BATS and HOT stations. These data were subsequently input into the OBPG visible band vicarious calibration system [7] to generate modeled SeaWiFS gain factors (Table 1). To explore the utility of a multisite calibration approach, we generated gains separately for the BATS and HOT sites and then assimilated both series for a combined solution (the validity of which is addressed later in this section). At this point, we have ORM-based $\bar{g}$ for comparison with the MOBY-based $\bar{g}$. Before proceeding with these comparisons, however, we review the accuracy and stability of our model-based $\bar{g}$.

To verify the accuracy of the calibration, we first incorporate the model-derived $\bar{g}$ into the OBPG satellite data product validation system [4] and calculate radiometric "matchup" statistics for the satellite and *in situ* observations used to derive $\bar{g}$ (Table 2). We acknowledge that this analysis does not validate the satellite retrievals, but the results provide some useful insight into the uncertainties associated with the gain determination. The average satellite-to-*in situ* mean ratios and biases approach unity and zero, respectively, as expected in a properly executed calibration, indicating that $\bar{g}$ accurately represents the central tendency of g_i for the series of calibration scenes. The absolute median percent differences, *MPD*, however, are approximately twice those reported by Franz *et al.* [7] for the MOBY-based calibration. The C_a climatologies represent the eight-year average seasonal cycle of each site. Day-to-day departures from these averages result in under- and overestimates of L_{wn}, and therefore g_i, which amplify our uncertainty in the derivation of $\bar{g}$. As expected, this additional uncertainty becomes apparent when comparing the ORM average matchup *MPD* with that from an *in situ* source that does not suffer from the same discrepancies (such as MOBY, as in Franz *et al.* [7]).

We next evaluate the temporal and geometric stability of the model-derived vicarious gains. The

Table 2. SeaWiFS Calibration Verification Statistics for the Scenes Used to Derive $\bar{g}$

	N	Ratio[a]	MPD[b]	RMS[c]	Bias[d]
$L_{wn}(412)$	90	1.007	4.4	0.111	0.016
$L_{wn}(443)$	90	1.005	3.4	0.084	0.014
$L_{wn}(490)$	90	1.006	2.9	0.042	0.010
$L_{wn}(510)$	90	1.008	2.9	0.029	0.009
$L_{wn}(555)$	90	1.021	5.0	0.020	0.006
$L_{wn}(670)$	90	1.067	20.0	0.008	0.003

[a]The median satellite-to-*in situ* ratio.
[b]The absolute median percent difference (relative to the *in situ* observations).
[c]The root mean square (standard deviation).
[d]The average signed difference between the satellite and *in situ* observations ($= \Sigma(satellite - in\ situ)/N$).

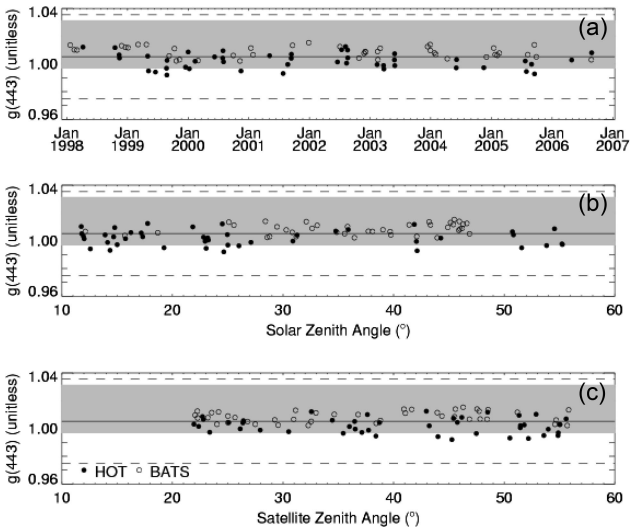

Fig. 7. SeaWiFS ORM-derived $g_i(443)$ as a function of time (a), solar zenith angle (b), and sensor zenith angle (c). The solid line indicates the final combined $\bar{g}(443)$ for the ORM, and the dashed lines delineate the boundary of $\bar{g} \pm 2\sigma$ (two standard deviations encompass ~95% of the data). Likewise, the shaded region demarks $\bar{g} \pm 2\sigma$ for MOBY. Only g_i falling within the series semi-interquartile range are shown (symbols), as we limit the final calculation of $\bar{g}$ to these data.

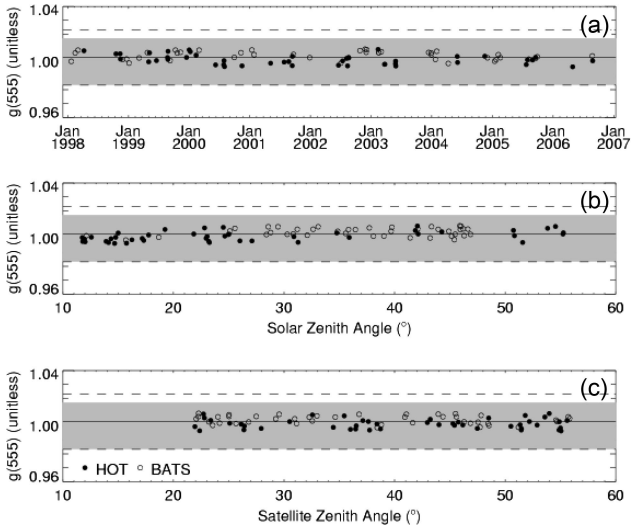

Fig. 8. SeaWiFS ORM-derived $g_i(555)$ as a function of time (a), solar zenith angle (b), and sensor zenith angle (c). The solid line indicates the final combined $\bar{g}(555)$ for the SSR model, and the dashed lines delineate the boundary of $\bar{g} \pm 2\sigma$ (two standard deviations encompass ~95% of the data). Likewise, the shaded region demarks $\bar{g} \pm 2\sigma$ for MOBY. Only g_i falling within the series semi-interquartile range are shown (symbols), as we limit the final calculation of $\bar{g}$ to these data.

g_i from both BATS and HOT do not demonstrate discernible trends as a function of time, long-term or seasonally [Figs. 7(a) and 8(a)]. If we consider SeaWiFS to be temporally stable, as has been demonstrated repeatedly [7,8], this suggests that our annual C_a climatologies adequately represent both sites, which would otherwise add irregular seasonality. Similarly, g_i from both BATS and HOT are consistent with (i.e., independent of) both solar and satellite zenith angles [Figs. 7(b), 7(c), 8(b), and 8(c)]. While not evident in these trends, variations with geometry are often symptomatic of problems with the atmospheric correction algorithm or the calculation

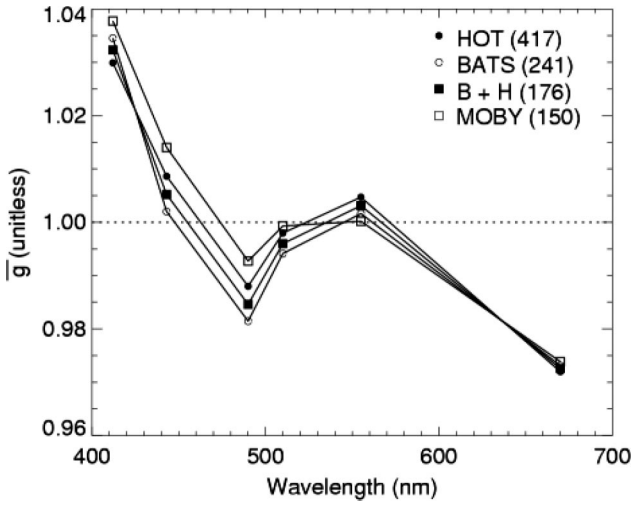

Fig. 9. Spectral distribution of $\bar{g}$ for MOBY and the ORM.

Table 3. Percent Differences[a] Between the MOBY and ORM $\bar{g}$

	412	443	490	510	555	670
BATS	−0.31	−1.18	−1.14	−0.52	0.14	−0.07
HOTS	−0.74	−0.53	−0.48	−0.14	0.44	−0.21
BATS + HOTS	−0.52	−0.86	−0.81	−0.33	0.29	−0.13

[a]Calculated using $(\bar{g}_{\mathrm{ORM}} - \bar{g}_{\mathrm{MOBY}}) \times 100\%/\bar{g}_{\mathrm{MOBY}}$.

of "exact" L_{wn} [16] within the vicarious calibration procedure.

For the BATS site, the MOBY- and model-derived $\bar{g}$ agree to within approximately ±0.5%, with the exception of 443 and 490 nm, whose absolute differences slightly exceed 1%. The $\bar{g}$ from the HOT site agree to within a similar range, with the exception of 412 nm (Fig. 9 and Table 3). Seemingly, these differences are minor, but as the atmosphere contributes a major portion of the radiance measured at the sensor (~90%), changes of this magnitude are in fact considerable (~5%) with respect to derived L_{wn} [54], as will be explored further in Section 5. Only the HOT $\bar{g}(510)$ and BATS and HOT $\bar{g}(670)$ are statistically equal to MOBY using a parametric Student's t analysis ($\alpha = 0.05$), but note that all sites have absolute differences on the order of the uncertainty of their derivation (i.e., standard deviation). Note also how the spectral shape of the difference (negative for the blue bands and positive for 555 nm) mirrors that of the field data comparisons we previously described.

Consider the following to put the magnitude of these differences in context: a reprocessing of the MOBY time series to correct for instrument stray light effects [55] resulted in changes in SeaWiFS $\bar{g}$ of ~1% on average (incorporated as part of SeaWiFS Reprocessing 4, July 2002). Furthermore, Franz *et al.* [7] illustrate absolute gain changes of 0.5% with increases in the sample size of g_i (i.e., increases in the number of calibration targets).

More notably, the BATS and HOT $\bar{g}$ agree to within ±0.66% in all bands (Table 4). The latter importantly underscores the viability of our approach, particularly considering the lack of regional tuning in the model that would presumably reduce the differences reported above. Relative to MOBY, both sites perform equally well, as the HOT $\bar{g}$ maintains better agreement (in terms of percent difference) for only three of the six spectral bands despite the geographic proximity of the HOT site and MOBY. We consider the portability of our approach to varied water masses to be an attractive feature that further assists in validating the model-driven calibration system. The remainder of our analyses make use of the combined BATS and HOT $\bar{g}$ (Table 1).

Table 4. Percent Differences[a] Between the HOT and BATS ORM $\bar{g}$

412	443	490	510	555	670
−0.44	0.66	0.66	0.38	0.30	−0.13

[a]Calculated using $(\bar{g}_{\mathrm{HOT}} - \bar{g}_{\mathrm{BATS}}) \times 100\%/\bar{g}_{\mathrm{BATS}}$.

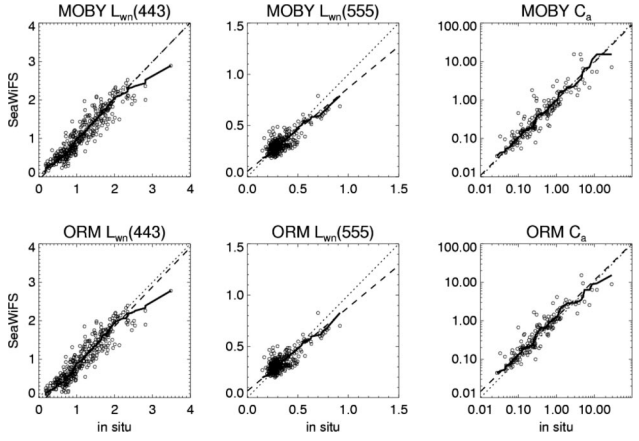

Fig. 10. SeaWiFS "matchup" validation results for $L_{wn}(443)$, $L_{wn}(555)$, and C_a for the MOBY (top row) and ORM (bottom row) derived $\bar{g}$. Data are limited to deep-water (>1000 m) stations and were acquired and processed following Bailey and Werdell [4]. The L_{wn} units are $\mu W\ cm^{-2}\ nm^{-1}\ sr^{-1}$ and the C_a units are $mg\ m^{-3}$. The dotted lines indicate a 1:1 relationship, the dashed lines show the comparisons' regressions, and the bold solid lines show quantile-quantile comparisons, where sorted (ascending order) *in situ* data are compared with sorted satellite data.

5. SeaWiFS Data Product Validation

Next, to evaluate the practical impact of using modeled $\bar{g}$ in lieu of that from MOBY, we input the recalculated gains into the OBPG satellite validation system [4] to generate SeaWiFS-to-*in situ* validation statistics for L_{wn} and C_a. These are subsequently compared with the operational SeaWiFS results. Figure 1 of Bailey and Werdell [4] provides a schematic overview of the validation process. We consider only deep-water stations (water depths >1000 m) in this analysis as they represent the majority of the global ocean and are generally not plagued with atmospheric correction failures (as are some coastal sites with absorbing aerosols, or other atmospheric conditions not currently represented by the existing aerosol correction scheme). C_a data were limited to those collected via HPLC.

The impact of the differences in $\bar{g}$ becomes immediately evident when comparing the MOBY and ORM validation results (Fig. 10 and Tables 5 and 6). Encouragingly, the regression slopes, coefficients of determination, and roots of the residual mean squares are nearly indistinguishable. The model-based *MPD* is slightly higher than that for MOBY, but is similar to within a few percent. The most obvious difference appears in the form of the mean satellite-to-*in situ* ratios, where yet again we see a relative decrease in the model-based blue bands and an increase in 555 nm. For the most part, the 510, 555, and 670 nm ratios are similar for both the MOBY and ORM runs, and one might further argue that the model-based calibration is statistically preferable at 555 nm. Yet, the 412, 443, and 490 nm ratios decrease by 7%–10%, which will have a noticeable consequence on the downstream calculation of C_a. As for the radiometric validation results, the C_a regression statistics and *MPD* are similar for the MOBY and ORM runs, but the satellite-to-*in situ* ratio increases by approximately 20% (from ~1 to ~1.2). Note, however, that both sets agree well near the annual global average [3] of ~0.25 $mg\ m^{-3}$.

We further validate the SeaWiFS data products through the generation of mission-long time-series of L_{wn} and C_a, following the methods outlined in Franz *et al.* [56] (reviewed in the caption of Fig. 11). Following the rationale previously described, we initially consider only deep-water pixels. In the interest of further evaluating temporal trends for distinct bioregimes, we also stratify the data into three trophic levels by adopting C_a values of 0.1 and 1 $mg\ m^{-3}$ as the approximate limits between oligotrophic and mesotrophic waters and between mesotrophic and eutrophic waters [57]. To facilitate the use of common geographic areas for both the MOBY and model-based processing, we use a mission long SeaWiFS C_a composite to define *a priori* the spatial boundaries of each trophic regime.

The radiometric validation statistics are bolstered by these time series comparisons (Fig. 11 and Table 7). As expected, the time series generated using the MOBY and model-based $\bar{g}$ produce identical seasonal trends and the differences in L_{wn} magnitudes are in the same direction as the differences in $\bar{g}$. We see, for

Table 5. SeaWiFS Validation Statistics for a Deep-Water Data Set (>1000 m) Using the MOBY-Derived $\bar{g}$

	N	Ratio (±SD)[a]	MPD[b]	Slope (±SE)[c]	r^2	RMSE[d]
$L_{wn}(412)$	197	0.996 (0.26)	11.9	1.09 (0.02)	0.92	0.212
$L_{wn}(443)$	332	0.949 (0.23)	15.1	1.03 (0.02)*	0.87	0.227
$L_{wn}(490)$	332	0.942 (0.18)	11.8	0.93 (0.02)	0.81	0.156
$L_{wn}(510)$	172	0.957 (0.16)	10.6	1.13 (0.07)*	0.55	0.103
$L_{wn}(555)$	332	0.974 (0.23)	15.0	0.71 (0.02)	0.83	0.060
$L_{wn}(670)$	320	1.375 (1.87)	70.7	1.06 (0.03)	0.59	0.021
C_a[e]	161	0.977 (0.93)	26.1	0.98 (0.03)*	0.87	0.529

[a]The median satellite-to-*in situ* ratio (with standard deviation).
[b]The absolute median percent difference (relative to the *in situ* observations).
[c]The slope of the reduced major axis linear regression (with standard error).
[d]The root of the residual mean square (in units equal to those of the observations).
[e]The C_a data were transformed prior to the regression analysis to account for their lognormal distribution.
*Indicates the slope and intercept (not shown) are statistically equal to 1 and 0, respectively, via a Student's t analysis at $\alpha = 0.05$.

Table 6. SeaWiFS Validation Statistics for the Data Set Presented in Table 5 Using the ORM-Derived $\bar{g}$

	N	Ratio (±SD)	MPD	Slope (±SE)	r^2	RMSE
$L_{wn}(412)$	197	0.924 (0.25)	12.4	1.08 (0.02)	0.92	0.213
$L_{wn}(443)$	332	0.843 (0.22)	18.4	1.02 (0.02)*	0.86	0.229
$L_{wn}(490)$	332	0.863 (0.17)	15.3	0.93 (0.03)	0.80	0.157
$L_{wn}(510)$	172	0.931 (0.16)	12.3	1.14 (0.08)*	0.55	0.104
$L_{wn}(555)$	332	1.018 (0.24)	15.6	0.72 (0.02)	0.82	0.061
$L_{wn}(670)$	320	1.325 (1.86)	69.0	1.07 (0.05)	0.59	0.022
C_a	161	1.232 (0.90)	30.1	0.96 (0.03)	0.87	0.475

*Indicates the slope and intercept (not shown) are statistically equal to 1 and 0, respectively, via a Student's t analysis at $\alpha = 0.05$.

example, that the −0.86% and 0.29% differences in $\bar{g}(443)$ and $\bar{g}(555)$, respectively, translate to differences of −7.3% and 4.1% in $L_{wn}(443)$ and $L_{wn}(555)$ in the deep-water subset (Table 7). Analogous radiometric differences are evident in the oligotrophic, mesotrophic, and eutrophic subsets. The model-to-MOBY time series ratios show the nine-year C_a averages to be 30%, 21%, 32%, and 25% higher for the deep-water, oligotrophic, mesotrophic, and eutrophic subsets, respectively (Table 7). Alas, seemingly minor differences in $\bar{g}$ relate to relevant changes in L_{wn} and therefore C_a. That said, the model-based deep-water C_a average more closely approaches the annual global average reported by Antoine *et al.* [3] (which, admittedly, includes eutrophic coastal regions). Ultimately, the use of the ORM-based $\bar{g}$ does not impact either the validation regressions (i.e., the slope and linearity over the observed dynamic range of observations), or the seasonality of the long-term time series, but rather introduces systematic biases in the results (Fig. 12).

Despite these results, differences in radiometry need not always translate to differences in C_a. In this regard, the direction of the change in the blue-band $\bar{g}$ relative to $\bar{g}(555)$ is more important than the combined magnitudes of the changes. The operational C_a algorithms for SeaWiFS and the Moderate Resolution Imaging Spectroradiometer (MODIS) relate sequencing ratios of blue-to-green R_{rs} to C_a in the form of a log-log sigmoidal curve such that a reduction in the R_{rs} ratio results in an increase in C_a. As was reported for the deep-water time-series, a ~7% decrease in $R_{rs}(443)$ and ~4% increase in $R_{rs}(555)$ incurs an ~11% decrease in their ratio, which translates to a ~30% increase in C_a (from approximately 1.8 to 2.3 mg m^{-3}). Consider next the typical R_{rs} ratios of 5.2, 1.8, and 1.05 as representative of our three defined trophic levels, which relate to C_a values of approximately 0.10, 0.5, and 2.0 mg m^{-3}. The reduction of these ratios by 11% leads to increases in C_a of 38%, 25%, and 17%, respectively. If we maintain the magnitude of the difference in $\bar{g}(555)$, but change its sign (representing a negative bias in lieu of a positive bias), the related changes in the R_{rs} ratios would be approximately −3%, which ultimately translates to increases in C_a of only 10%, 7%, and 5%, respectively, for the three trophic levels. Thus, we suggest that in the context of future calibration modeling efforts whose ultimate goal is the derivation of a C_a time-series that the L_{wn} spectral shape be potentially considered more significant in the derivation of the ORM than its overall magnitude.

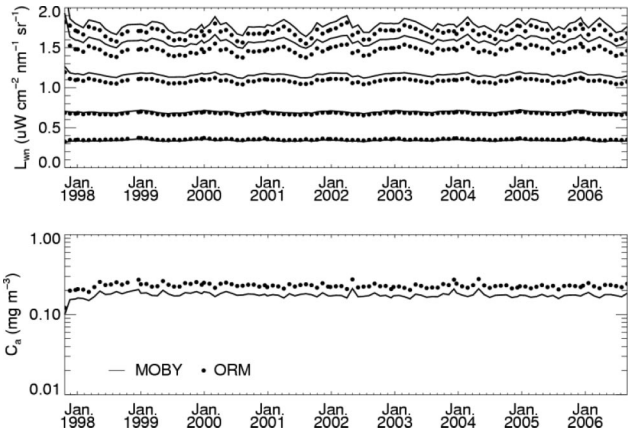

Fig. 11. Comparison of SeaWiFS L_{wn} (top) and C_a (bottom) trends for global deep water (>1000 m) using the MOBY (solid lines) and ORM (solid circles) derived $\bar{g}$. In the top panel, from top to bottom, the L_{wn} are 412, 443, 490, 510, and 555 nm. As described in Franz *et al.* [56], global level-3 daily L_{wn} and C_a files were generated, then spatially averaged into approximately 9-by-9 km resolution equal-area bins, then temporally averaged into four-day composites. To minimize data storage requirements and maximize computational efficiency, only one four-day composite per month is considered (i.e., four weeks separate each composite), leaving a total of 107 L_{wn} and C_a composites in the time-series.

6. Extension to CZCS and OCTS

We now review the applicability of our approach to retrospective analyses of the CZCS and OCTS time-series. Despite their demise in 1986 and 1997, respectively, both data sets continue to be extensively reviewed [3,14,58–60], particularly in the context of resolving decadal trends in global marine productivity [3]. The OBPG recently reanalyzed and reprocessed both the CZCS and OCTS data sets to conform their data processing methodology to that of SeaWiFS and MODIS (the goal being a consistently processed time series for all sensors). Such sensor continuity has long been a community goal [3,59] and we refer the reader to Table 1 of Antoine *et al.* [3] for a summary of previous CZCS reanalysis efforts. The details of the OBPG reprocessing efforts are provided elsewhere [61]; however, a review of how our modeling approach was incorporated into the OBPG on-

Table 7. Nine-Year Means for the SeaWiFS Deep-Water and Trophic Time-Series Generated Using the MOBY and ORM $\bar{g}$

	MOBY	ORM	Ratio[a]	MOBY	ORM	Ratio[a]
	Deep Water (>1000 m)			Mesotrophic ($0.1 \le C_a \le 1$ mg m^{-3})		
$L_{wn}(412)$	1.784 (0.074)	1.697 (0.075)	0.951 (0.003)	1.367 (0.052)	1.282 (0.053)	0.938 (0.004)
$L_{wn}(443)$	1.589 (0.052)	1.473 (0.054)	0.927 (0.004)	1.294 (0.039)	1.180 (0.041)	0.912 (0.005)
$L_{wn}(490)$	1.162 (0.022)	1.087 (0.023)	0.935 (0.003)	1.066 (0.027)	0.991 (0.029)	0.929 (0.004)
$L_{wn}(510)$	0.697 (0.012)	0.678 (0.012)	0.972 (0.001)	0.700 (0.017)	0.680 (0.018)	0.972 (0.002)
$L_{wn}(555)$	0.340 (0.008)	0.353 (0.008)	1.041 (0.001)	0.367 (0.010)	0.381 (0.010)	1.040 (0.002)
$L_{wn}(670)$	0.043 (0.002)	0.042 (0.002)	0.977 (0.002)	0.047 (0.002)	0.046 (0.002)	0.978 (0.002)
C_a	0.176 (0.014)	0.229 (0.019)	1.304 (0.014)	0.246 (0.015)	0.324 (0.022)	1.321 (0.017)
	Oligotrophic ($C_a < 0.1$ mg m^{-3})			Eutrophic ($C_a > 1$ mg m^{-3})		
$L_{wn}(412)$	2.454 (0.131)	2.364 (0.132)	0.963 (0.003)	0.510 (0.054)	0.445 (0.053)	0.872 (0.011)
$L_{wn}(443)$	2.073 (0.090)	1.955 (0.092)	0.943 (0.004)	0.689 (0.060)	0.590 (0.058)	0.856 (0.012)
$L_{wn}(490)$	1.330 (0.026)	1.256 (0.028)	0.944 (0.003)	0.873 (0.073)	0.806 (0.073)	0.922 (0.006)
$L_{wn}(510)$	0.706 (0.010)	0.686 (0.010)	0.972 (0.001)	0.840 (0.073)	0.822 (0.073)	0.979 (0.002)
$L_{wn}(555)$	0.307 (0.008)	0.320 (0.008)	1.042 (0.001)	0.768 (0.080)	0.787 (0.080)	1.026 (0.003)
$L_{wn}(670)$	0.038 (0.003)	0.037 (0.003)	0.976 (0.004)	0.163 (0.030)	0.162 (0.030)	0.996 (0.002)
C_a	0.069 (0.007)	0.084 (0.008)	1.213 (0.010)	2.213 (0.211)	2.756 (0.253)	1.246 (0.022)

[a]ORM-to-MOBY ratio.

orbit calibration effort is provided in this section, along with a brief CZCS and OCTS calibration history.

Attempts to vicariously calibrate CZCS began shortly after launch, when inconsistencies in the water-leaving radiances and derived products began to prevail [54,62] and degradation in the instrument sensitivity was routinely observed [63]. Evans and Gordon [14] (EG94) performed a full retrospective analysis of the CZCS calibration and derived updated $\bar{g}$ and temporal degradation factors for its four ocean color bands. Briefly, bands 2 and 3 (520 and 550 nm) were calibrated by repeatedly processing the full CZCS data archive using revised calibration coefficients until the modes of 10-day histograms of $L_{wn}(520)$ and $L_{wn}(550)$ for global Case-1 waters remained temporally stable over the life of the mission and centered on the typical oligotrophic values of 0.5 and 0.3 mW cm^{-2} um^{-1} sr^{-1}, respectively. Band 1 (443 nm) was calibrated through forced agreement with *in situ* radiometric and pigment data collected by the Nimbus Experiment Team (the CZCS-derived pigment values were forced to agree with the ship-determined values when radiometry was unavailable). EG94 minimally calibrated band 4 (670 nm), minus a small degradation introduced in late 1982. Subsequent reanalyses [3,59] used the EG94 results, with the exception of an accelerated band 4 temporal degradation.

Given that CZCS lacked onboard calibration capabilities, and considering that the current standard temporal degradation model was vicariously determined (EG94 for bands 1–3 and Antoine *et al.* [3] for band 4), we explored the feasibility of applying our modeling approach to derive the temporal degradation of the instrument. CZCS acquired sufficient temporal coverage of the Sargasso Sea to allow application of our BATS climatology [61] (recall also that this climatology was reproduced using historical C_a from the WOD05; see Fig. 5). Unlike modern sensors with functional NIR channels, CZCS requires the use of band 4 and some assumption or ancillary knowledge of aerosol type to estimate both the aerosol and water-leaving radiance contributions to the top-of-atmosphere radiance at 670 nm. To start, we adopted the OBPG vicarious calibration approach [7] and retained only the instrument prelaunch calibration. We then determined the temporal calibration of band 4 based on modeled $L_{wn}(670)$ and estimated aerosol reflectances, where the latter were derived from SeaWiFS climatological aerosol optical thickness and Angstrom exponent retrievals at BATS using the approach outlined by Franz *et al.* [64]. We then reprocessed the CZCS series at BATS using this band 4 temporal degradation, modeled L_{wn}, and the assumed maritime aerosol model to derive a time-series of gains for bands 1–3. This was done only for the first CZCS gain setting. Encouragingly, such an approach appears to be practicable given the agreement of the modeled gain time-series with that reported in EG94 (Fig. 13). Despite this, not wishing to tie the CZCS on-orbit calibration to SeaWiFS aerosol retrievals or to insert additional uncertainties based on the required aerosol assumptions, the OBPG ultimately opted to use the EG94 temporal degradations for its reprocessing effort.

We therefore adopted the EG94 temporal calibration for all CZCS bands and, additionally, the EG94 absolute band 4 gain of 1.008 (for the first gain setting), and rederived $\bar{g}$ for bands 1–3 using the modeled target L_{wn} from the BATS site and OBPG vicarious calibration approach [7]. In doing so, we assumed a constant maritime aerosol model to extrapolate the aerosol contributions from 670 nm to the shorter wavelengths, which is consistent with the operational approach used by the OBPG. As alluded to in the previous paragraph, the absence of multiple CZCS near-infrared bands prohibits aerosol model selection as is currently done for modern sensors [1].

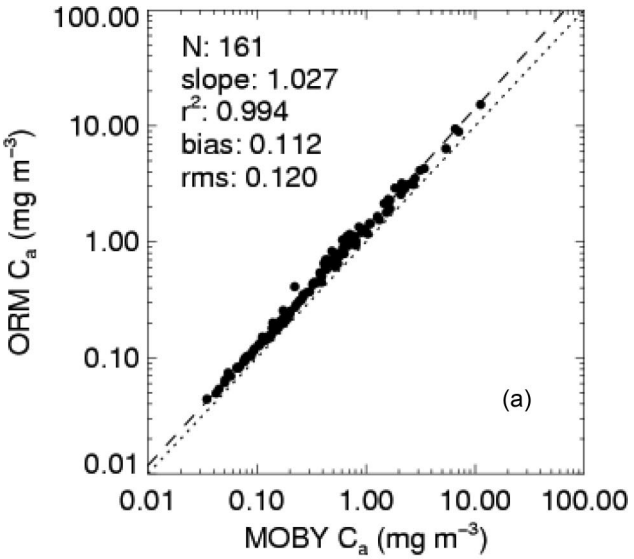

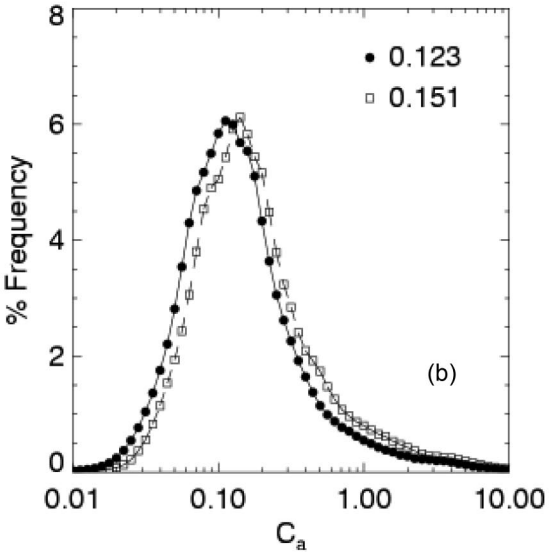

Fig. 12. For (a), a comparison of common SeaWiFS C_a validation "matchups" retrieved using the MOBY and ORM derived $\bar{g}$. The sample size (*N*), regression slope (*slope*) and correlation coefficient (r^2), bias (*bias*), and root mean square (*rms*) are provided. The dotted line indicates a 1:1 relationship and the dashed line shows the comparison's regression. For (b), the relative distributions of C_a, in percent frequency, for common bins in a four-day composite (August 2005) processed using the MOBY (solid circles) and ORM (open squares) derived $\bar{g}$. The statistical mode for each is also provided.

The OBPG decision to assign a constant aerosol type within CZCS processing is debatable, as more ambitious approaches have been implemented elsewhere [3,59,62,65]. Our current intent, however, is simply to demonstrate the value of a temporally varying ORM in vicarious calibration, and therefore a detailed discussion of CZCS atmospheric correction is beyond the scope of this analysis. Note also that we ultimately limited the determination of $\bar{g}$ to data collected prior to 1982, as uncertainties associated with the appearance of an El Niño, the eruption of El Chichón, and a late-mission instrument heating event [66] inhibited

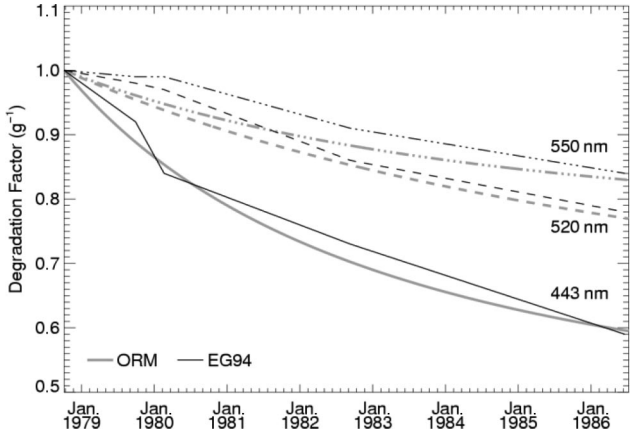

Fig. 13. Temporal degradation of CZCS bands 1–3 as derived by EG94 (thin black lines) and by the ORM (thick gray lines). Solid lines denote band 1 (443 nm), dashed lines denote band 2 (520 nm), and dotted-dashed lines denote band 3 (550 nm).

our confidence in post-1981 CZCS data processing. Like the temporal calibration results, the model-based $\bar{g}$ (Table 8) agreed favorably with those reported in EG94, further corroborating the approach.

As it was for CZCS, few *in situ* radiometric measurements were collected during the OCTS era (which ended prematurely after only nine months of data collection). NASDA opted to calibrate OCTS vicariously by forcing the satellite measurements to match this limited series of field observations. Initially, it used a single radiometric profile and ancillary atmospheric measurements collected off the coast of California to calibrate its six visible and two NIR bands [67]. NASDA later recalibrated the two NIR bands (bands 7 and 8) using eight clear satellite scenes with known aerosol types (i.e., aerosol models) and an assumption of perfect prelaunch calibration for band 6 (670 nm). The remaining five visible bands were recalibrated using two spectra from the Yamata Bank Optical Moored buoy system. In contrast, Gregg *et al.* [58] assumed perfect prelaunch calibration for band 8 (865 nm) and recalibrated band 7 (765 nm) using OCTS scenes contaminated by Sun glint, where they could assume a lack of spectral dependence between 765 and 865 nm. They recalibrated the visible bands using six *in situ* radiometric profiles collected in the New York Bight, Gulf of Maine, and off Lanai. Most recently, Wang *et al.* [60] adopted the NASDA band 8 (865 nm) calibration, but proceeded with the band 7 (765 nm) and visible band calibration following Eplee *et al.* [6], including the sole use of MOBY radiometry (six measurements col-

Table 8. CZCS $\bar{g}$ and Standard Deviations[a] (in Parentheses) Calculated Using the ORM at the BATS Site

N	443	520	550	670
7	1.0094 (0.031)	0.9525 (0.019)	0.9543 (0.024)	1.008 (NA)

[a]With the exception of 670 nm, as the EG94 value was adopted for our analysis.

Table 9. OCTS $\bar{g}$ and Standard Deviations (in Parentheses) Calculated Using the ORM at the BATS and HOT Sites

N	412	443	490	520	565	670
45	1.1684 (0.016)	1.0453 (0.014)	0.9867 (0.013)	1.0294 (0.011)	1.0370 (0.010)	1.0567 (0.015)

lected from late November 1996 to late February 1997). Note that an on-orbit temporal calibration of OCTS has yet to be applied.

The OBPG vicarious calibration of the OCTS NIR bands is described elsewhere [61], but follows that described in Franz *et al.* [7]. Consistent temporal coverage of the BATS and HOT sites by OCTS permitted the OBPG to use modeled L_{wn} from both in its vicarious recalibration effort [61]. As was described for SeaWiFS in Section 4, we derived model-based $\bar{g}$ for the six visible OCTS bands (Table 9), all of which generally agree in magnitude with those reported by Shimada *et al.* [67], Gregg *et al.* [58], and Wang *et al.* [60]. As these latter studies made use of very limited and varied *in situ* data sets, we naturally expect some differences. In its OCTS processing, the OBPG removed a tilt-dependent instrument gain setting and applied bilinear temporal degradations to the NIR bands (765 and 865 nm). The details of these are provided elsewhere [61], but they are worth highlighting briefly as both contribute to the differences in $\bar{g}$ mentioned above. For OCTS, one advantage of the model-based calibration approach is the increased statistical sample size, which, as shown in Franz *et al.* [7], decreases the uncertainty associated with the derived vicarious gains. Note also that our derived gains compare well with the clear-water model-based vicarious gains reported in Gregg *et al.* [58].

To evaluate the practical utility of the model-derived vicarious gains, we generated CZCS and OCTS L_{wn} and C_a satellite-to-*in situ* validation results [4], as was done for SeaWiFS in Section 5. We obtained global CZCS-era C_a measurements from the WOD05 [13] and radiometric observations from SeaBASS. While the C_a span from November 1978 through May 1986, the radiometry is limited to a series of three cruises conducted from November 1978 to June 1979 [66], representing, to our knowledge, the only CZCS-era radiometry that have been made publicly available. Global OCTS-era pigments and radiometric data were both acquired from SeaBASS and include the 1996 preoperations MOBY deployment. In preparation for the validation activity, all data were treated following Werdell and Bailey [39]. In contrast to that described in Section 5, however, these data were not limited to deep water (>1000 m) stations, and only fluorometrically derived C_a were available for both satellite missions.

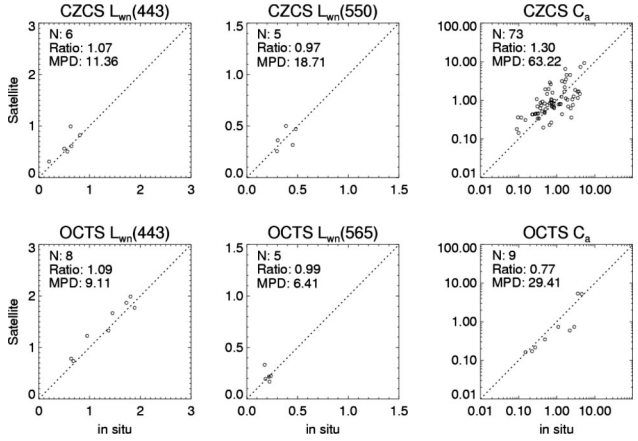

Fig. 14. Validation results for CZCS and OCTS L_{wn} and C_a. The sample size (*N*), satellite-to-*in situ* ratio (*Ratio*), and absolute median percent difference relative to the *in situ* measurement (*MPD*) are provided in each panel. The dotted lines indicate a 1:1 relationship. The L_{wn} units are $\mu W\ cm^{-2}\ nm^{-1}\ sr^{-1}$ and the C_a units are $mg\ m^{-3}$.

Despite the diminutive sample sizes, the radiometric matchups are favorable for both CZCS and OCTS (Fig. 14), reporting satellite-to-*in situ* ratios that approach unity and *MPD* that paralleled or exceeded the SeaWiFS results. The CZCS C_a maintain high *MPD*, partly because of the mid-to-late mission uncertainties listed above, but are otherwise fairly well-represented over the dynamic range of 0.1 to 10 $mg\ m^{-3}$. With the exception of two outliers, the OCTS C_a matchups all also closely agree. The paucity of radiometric data for both CZCS and OCTS prohibits the robust correlation of radiometric error into the C_a matchups (as was attempted in Section 5). The OBPG operational CZCS C_a algorithm mimics the construction of that for SeaWiFS [2]. Following the logic we presented earlier, one might interpret the satellite-to-*in situ* C_a ratio of 1.3 to indicate either $R_{rs}(443)$ to be low or $R_{rs}(550)$ to be high, neither of which appears to be the case in Fig. 14. Overall, however, given the combined uncertainties associated with the C_a climatologies, the ORM, the historical *in situ* data sets, and CZCS and OCTS systems themselves (their characterization and atmospheric correction approach), we conclude these satellite-to-*in situ* validation results to be rather encouraging. Despite this, a multitude of other calibration and data processing concerns [61] currently inhibit either sensor's viability as a resource for long-term climate research.

7. Discussion

In this paper, we explored using an ocean surface reflectance model to calibrate vicariously SeaWiFS in lieu of *in situ* data, with the long-term goal of developing a modern baseline technique for the calibration of the visible bands of CZCS and OCTS. In particular, we intended to provide both the technical and analytical foundation for such an approach and, building on Franz *et al.* [7], a first-order analysis of the uncertainties associated with changes in visible vicarious

gain coefficients as they relate to the development of decadal C_a climate data records. We reiterate that our approach is not intended to replace the use of *in situ* radiometers, for example MOBY and other existing calibration-quality instrument networks [68], but rather to provide a viable calibration alternative, or complement, in the absence of abundant coincident field data, as is the case for both CZCS and OCTS.

Using an ocean surface reflectance model [11,16] that has been shown to be valid in Case-1 waters, SeaWiFS vicarious gains were recalculated to within $\pm 0.9\%$ of that from MOBY for all six visible bands, with only $\bar{g}(443)$ and $\bar{g}(490)$ exceeding 0.5% absolute difference (Table 1). The $\bar{g}$ for BATS and HOT sites are also within $\pm 0.7\%$ of each other, verifying the portability of the model (Table 4). Ostensibly, these results are remarkably good given that they were acquired using modeled annual C_a expressions for two different water masses and a globally parameterized ORM (all of which have compounding uncertainties). Despite the small differences, however, we suspect the ORM-C_a climatology combination produces L_{wn} that are subtly, yet overly, spectrally flat (too low at blue wavelengths and too high at green wavelengths), at least in its current form. This is first detectable through temporal comparisons of modeled output with *in situ* radiometric observations, where the C_a climatology provides input into the ORM (Fig. 6). Later, the spectral dependency becomes clearly recognizable in the SeaWiFS L_{wn} validation satellite-to-*in situ* ratios (Table 6). With regards to derived products, the net effect of the spectral differences in $\bar{g}$ is a 30% increase in global C_a, as represented by our deep-water (>1000 m) SeaWiFS subset. At this stage, however, we do not presuppose that either the ORM or annual C_a expressions is singularly responsible for the differences between modeled and MOBY $\bar{g}$.

It is worth recalling that this C_a-based bio-optical model relies on average empirical relationships for Case-1 waters, specifically Eqs. (3) and (6), so that the resulting radiances provide only the average spectra for the given C_a used as input. Actually, the natural variability of the bio-optical properties of Case-1 waters introduces considerable scatter around these relationships (see, e.g., Fig. 3 of Loisel and Morel [19] and Fig. 3 of MM01), and therefore some uncertainties inevitably affect the predicted radiance spectra. Further, we cannot ignore that some systematic differences may temporarily or permanently exist in certain geographic zones, even if they are identified as Case-1 waters. The Mediterranean Sea provides an example of this particular behavior [69]. The Sargasso Sea also experiences seasonal fluctuations in the components of marine absorption [50].

Seemingly, the use of regionally acquired *in situ* measurements would locally improve the empirical expressions within the ORM and assist in the validation of the remaining analytically derived components. Currently, the radiometric and biological parameters required to reconstruct Eqs. (3) and (6) are routinely collected by most marine observational programs using commercially available instrumentation. If the standard suite of radiometric profiles (upwelling radiance and downwelling irradiance) were to be expanded to include upwelling irradiance (possible by positioning the irradiance sensor to point to nadir), routine measurements of nadir Q are also feasible using existing technology (many field programs have already adopted this approach). We used a limited suite of regional observations to diagnose problematic empirical expressions within the ORM. While a complete reparameterization of these expressions was appealing, in practice their statistical rederivation proved challenging because of the limited dynamic range in C_a and the other products of interest.

Despite its current lack of regional tuning, we find the demonstrated portability of the ORM calibration approach to be one of its more appealing features. The results presented in Tables 3 and 4 indicate convergence between not only the BATS and HOT $\bar{g}$ with MOBY, but also with each other. In its current (globally parameterized) state, the approach is geographically limited only by the availability of reliable long-term C_a time-series. When C_a is unavailable, the approach is economically limited only by the cost of collecting and processing phytoplankton pigments. In this context of economic feasibility, our model-based approach provides a cost-effective alternative for vicarious calibration when compared to what is required to develop and maintain an autonomous mooring or marine platform. Even were regional tuning deemed necessary, the field instrumentation is limited to those needed to evaluate and update the empirical components of the ORM (e.g., commercially available radiometers and transmissometers), as we described.

We are not suggesting that the model-based approach be used in lieu of field radiometry to calibrate modern ocean color satellite instruments in the presence of abundant, high quality *in situ* data. The SeaWiFS L_{wn} and C_a validation results (Fig. 10 and Tables 5 and 6) are clearly superior for the MOBY-derived $\bar{g}$. An emerging body of evidence also exists in support of prerequisite radiometric accuracy for vicarious calibration of ocean color sensors that cannot currently be achieved by the ORM [70]. Rather, we propose that the modeling approach be considered when field radiometry is unavailable, such as for historical missions, or impractical, as would be the case for a recently launched satellite instrument. Franz *et al.* [7] demonstrated that a minimum of 30–40 g_i are required to satisfactorily derive $\bar{g}$. For a recently launched satellite, for example, our approach provides a complementary source of target L_{wn} when field data are still being acquired or reviewed or as a supplement to an *in situ* time-series to increase the statistical sample size.

While we highlight the utility of the ORM for ocean color satellite calibration, it also provides a viable mechanism for radiometric validation in the absence of *in situ* data. As a case study, consider the early-mission performance of the NASA MODIS onboard the Aqua spacecraft, which was launched in early

2002. Prior to 2004, the derived ocean color products demonstrated a strong latitudinal dependency, which partly stemmed from an incorrect interpretation of the prelaunch characterization of the instrument polarization [71]. This dependency was not fully evident until the MODIS radiometry was compared with SeaWiFS products at high latitudes [56], as few field radiometric measurements were available to diagnose such a problem. In such a data-poor scenario, the ORM provides a complementary source of plausible L_{wn}.

The ORM calibration approach might be further extended to support analytical studies concerning future instrument design and deployment strategies. For example, the ORM provides an opportunity to quantify the minimum resolution required to maintain acceptable levels of uncertainty in $\bar{g}$, if subnanometer resolution (as for MOBY) proves too costly to maintain in the future. The ORM approach also provides a mechanism to evaluate the costs and benefits of developing and maintaining multiple, geographically varied calibration sites prior to deploying autonomous instrumentation. Franz *et al.* [7] suggest that remotely sensed L_w retrievals in coastal and inland waters are likely to exhibit systematic biases caused by regionally specific errors in the atmospheric correction process (e.g., localized aerosol conditions). In the absence of radiometric field data, a regionally tuned ORM can provide a cost-effective mechanism for adjusting the remote sensing system to improve the performance of L_w retrievals in such locations.

Here, however, our primary interest is continuity among historical and current ocean color satellite data products. Within the practical context of CZCS and OCTS reprocessing—that is, the generation of decadal C_a climate data records—the absolute radiometric calibration is less significant provided the derived multisensor C_a are accurate and without instrument-to-instrument biases. If radiometric accuracy were to be moderately sacrificed for consistently derived C_a, this would be accomplished using a systematic reprocessing of the relevant ocean color satellites with a consistent vicarious calibration target, such as the ORM. Our intent was simply to develop the methodology and build the analytical framework for a modern model-based vicarious calibration approach. We quantified the ability of our model-based approach to replicate MOBY vicarious gains for SeaWiFS, and subsequently derived CZCS and OCTS gains of equal or superior value to those currently available. Ultimately, the proximity of the SeaWiFS model-based $\bar{g}$ to that from MOBY is very encouraging (less than absolute 0.9% spectrally), and will be improved upon with additional insight into the absorption and scattering properties of various optically relevant marine constituents.

This paper was funded by the NASA Earth Observing System (EOS)/MODIS Program. We thank Stan Hooker and Watson Gregg for their valuable comments on various stages of this body of work. We also thank two anonymous reviewers for their comments. We are grateful to Wayne Robinson, Fred Patt, Joel Gales, and Gene Feldman for their efforts in these latest CZCS and OCTS reprocessing efforts. We also thank the members of the BATS and HOT observational programs, including David Siegel, Norman Nelson, Ricardo Letelier, and Jasmine Nahorniak, for the radiometric measurements, without which this work would not have been possible.

References

1. H. R. Gordon and M. H. Wang, "Retrieval of water-leaving radiance and aerosol optical-thickness over the oceans with SeaWiFS—a preliminary algorithm," Appl. Opt. **33,** 443–452 (1994).
2. J. E. O'Reilly, S. Maritorena, B. G. Mitchell, D. A. Siegel, K. L. Carder, S. A. Garver, M. Kahru, and C. R. McClain, "Ocean color chlorophyll algorithms for SeaWiFS," J. Geophys. Res. **103,** 24937–24954 (1998).
3. D. A. Antoine, A. Morel, H. R. Gordon, V. F. Banzon, and R. H. Evans, "Bridging ocean color observations of the 1980s and 2000s in search of long-term trends," J. Geophys. Res. **110,** doi:10.1029/2004JC002620 (2005).
4. S. W. Bailey and P. J. Werdell, "A multi-sensor approach for the on-orbit validation of ocean color satellite data products," Remote Sen. Environ. **102,** 12–23 (2006).
5. H. R. Gordon, "In-orbit calibration strategy for ocean color sensors," Remote Sens. Environ. **63,** 265–278 (1998).
6. R. E. Eplee, Jr., W. D. Robinson, S. W. Bailey, D. K. Clark, P. J. Werdell, M. Wang, R. A. Barnes, and C. R. McClain, "Calibration of SeaWiFS. II. Vicarious techniques," Appl. Opt. **40,** 6701–6718 (2001).
7. B. A. Franz, S. W. Bailey, P. J. Werdell, and C. R. McClain, "Sensor-independent approach to the vicarious calibration of satellite ocean color radiometry," Appl. Opt. **46,** 5068–5082 (2007).
8. R. A. Barnes, R. E. Eplee Jr., F. S. Patt, H. H. Kieffer, T. C. Stone, G. Meister, J. J. Butler, and C. R. McClain, "Comparison of SeaWiFS measurements of the Moon with the U.S. Geological Survey lunar model," Appl. Opt. **43,** 5838–5854 (2004).
9. D. K. Clark, H. R. Gordon, K. J. Voss, Y. Ge, W. Broenkow, and C. Trees, "Validation of atmospheric correction over oceans," J. Geophys. Res. **102,** 17209–17217 (1997).
10. H. R. Gordon, O. B. Brown, R. H. Evans, J. W. Brown, R. C. Smith, K. S. Baker, and D. K. Clark, "A semianalytic radiance model of ocean color," J. Geophys. Res. **93,** 10909–10924 (1988a).
11. A. Morel and S. Maritorena, "Bio-optical properties of oceanic waters: a reappraisal," J. Geophys. Res. **106,** 7163–7180 (2001).
12. A. Morel and L. Prieur, "Analysis of variations in ocean color," Limnol. Oceanogr. **22,** 709–722 (1977).
13. T. P. Boyer, J. I. Antonov, H. E. Garcia, D. R. Johnson, R. A. Locamini, A. V. Mishonov, M. T. Pitcher, O. K. Baranova, and I. V. Smolyar, *World Ocean Database 2005,* S. Levitus, ed., NOAA Atlas NESDIS 60 (U.S. Government Printing Office, 2006).
14. R. H. Evans and H. R. Gordon, "Coastal zone color scanner 'system calibration': a retrospective examination," J. Geophys. Res. **99,** 7293–7307 (1994).
15. H. R. Gordon, O. B. Brown, and M. M. Jacobs, "Computed relationships between the inherent and apparent optical properties of a flat homogeneous ocean," Appl. Opt. **14,** 417–427 (1975).
16. A. Morel, D. Antoine, and B. Gentili, "Bidirectional reflectance of oceanic waters: accounting for Raman emission and varying

particle scattering phase function," Appl. Opt. **41,** 6289–6306 (2002).
17. H. R. Gordon, "Normalized water-leaving radiance: revisiting the influence of surface roughness," Appl. Opt. **44,** 241–248 (2005).
18. A. Morel and J. L. Mueller, "Normalized water-leaving radiance and remote sensing reflectance: bidirectional reflectance and other factors," in *Ocean Optics Protocols for Satellite Ocean Color Sensor Validation, Revision 4, Vol. III: Radiometric Measurements and Data Analysis Protocols,* J. L. Mueller, G. S. Fargion, and C. R. McClain, eds. (NASA Goddard Space Flight Center, 2003), pp. 32–59.
19. H. Loisel and A. Morel, "Light scattering and chlorophyll concentration in case 1 waters: a reexamination," Limnol. Oceanogr. **43,** 847–858 (1998).
20. D. Stramski, E. Boss, D. Bogucki, and K. J. Voss, "The role of seawater constituents in light backscattering in the ocean," Prog. Oceanogr. **61,** 27–56 (2004).
21. M. S. Twardowski, E. Boss, J. B. Macdonald, W. S. Pegau, A. H. Barnard, and J. R. V. Zaneveld, "A model for estimating bulk refractive index from the optical backscattering ratio and the implications for understanding particle composition in case I and case II waters," J. Geophys. Res. **106,** 14129–14142 (2001).
22. E. Boss, W. S. Pegau, M. Lee, M. Twardowski, E. Shybanov, G. Korotaev, and F. Baratange, "Particulate backscattering ratio at LEO 15 and its use to study particle composition and distribution," J. Geophys. Res. **109,** doi:10.1029/2002JC001514 (2004).
23. J. M. Sullivan, M. S. Twardowski, P. L. Donaghay, and S. A. Freeman, "Use of optical scattering to discriminate particle types in coastal waters," Appl. Opt. **44,** 1667–1680 (2005).
24. Y. Ahn, A. Bricaud, and A. Morel, "Light backscattering efficiency and related properties of some phytoplankters," Deep-Sea Res., Part A **39,** 1835–1855 (1992).
25. D. Stramski and D. A. Kiefer, "Light scattering by microorganisms in the open ocean," Prog. Oceanogr. **28,** 343–383 (1991).
26. D. A. Caron, H. G. Dam, P. Kremer, E. J. Lessard, L. P. Madin, T. C. Malone, J. M. Napp, E. R. Peele, M. R. Roman, and M. J. Youngbluth, "The contribution of microorganisms to particulate carbon and nitrogen in surface waters of the Sargasso Sea near Bermuda," Deep-Sea Res., Part I **42,** 943–972 (1995).
27. D. M. Karl, "A sea of change: biogeochemical variability in the North Pacific subtropical gyre," Ecosystems **2,** 181–214 (1999).
28. A. M. Ciotti, J. J. Cullen, and M. R. Lewis, "A semi-analytical model of the influence of phytoplankton community structure on the relationship between light attenuation and ocean color," J. Geophys. Res. **104,** 1559–1578 (1999).
29. H. Loisel, J.-M. Nicolas, A. Sciandra, D. Stramski, and A. Poteau, "Spectral dependency of optical backscattering by marine particles from satellite remote sensing of the global ocean," J. Geophys. Res. **111,** doi:10.1029/2005JC003367 (2006).
30. A. Bricaud, H. Claustre, J. Ras, and K. Oubelkheir, "Natural variability of phytoplankton absorption in oceanic waters: influence of the size structure of algal populations," J. Geophys. Res. **109,** doi:10.1029/2004JC002419 (2004).
31. A. Bricaud, A. Morel, M. Babin, K. Allali, and H. Claustre, "Variations of light absorption by suspended particles with chlorophyll a concentration in oceanic (case 1) waters: analysis and implications for bio-optical models," J. Geophys. Res. **103,** 31,033–31,044 (1998).
32. D. A. Siegel, S. Maritorena, N. B. Nelson, M. J. Behrenfeld, and C. R. McClain, "Colored dissolved organic matter and its influence on the satellite-based characterization of the ocean biosphere," Geophys. Res. Lett. **32,** doi:10.1029/2005GL024310 (2005).
33. L. Prieur and S. Sathyendranath, "An optical classification of coastal and oceanic waters based on the specific absorption curves of phytoplankton pigments, dissolved organic matter, and other particulate materials," Limnol. Oceanogr. **26,** 671–689 (1981).
34. A. Bricaud, A. Morel, and L. Prieur, "Absorption by dissolved organic matter of the sea (yellow substance) in the UV and visible domains," Limnol. Oceanogr. **26,** 43–53 (1981).
35. M. S. Twardowski, E. Boss, J. M. Sullivan, and P. L. Donaghay, "Modeling the spectral shape of absorption by chomophoric dissolved organic matter," Mar. Chem. **89,** 69–88 (2004).
36. H. R. Gordon, "Dependence of diffuse reflectance of natural waters on the Sun angle," Limnol. Oceanogr. **34,** 1484–1489 (1989).
37. A. Morel and B. Gentili, "Radiation transport within oceanic (case 1) water," J. Geophys. Res. **109,** doi:10/1029/2003JC002259 (2004).
38. P. J. Werdell, S. Bailey, G. Fargion, C. Pietras, K. Knobelspiesse, G. Feldman, and C. R. McClain, "Unique data repository facilitates ocean color satellite validation," EOS Trans. AGU **84,** 379 (2003).
39. P. J. Werdell and S. W. Bailey, "An improved *in situ* bio-optical data set for ocean color development and satellite data product validation," Remote Sens. Environ. **98,** 122–140 (2005).
40. A. V. Mishonov and W. D. Gardner, "Assessment and correction of the historical beam attenuation data from HOT—ALOHA & BATS stations," Oceanogr. **16,** 51 (2003).
41. S. B. Hooker, Hydrospheric and Biospheric Science Laboratory, NASA Goddard Space Flight Center, 614.8, Greenbelt, Maryland 20771 USA (personal communication, 2007).
42. K. J. Voss and A. Morel, "Bidirectional reflectance function for oceanic waters with varying chlorophyll concentrations: measurements versus prediction," Limnol. Oceanogr. **50,** 698–705 (2005).
43. M. J. Behrenfeld and E. Boss, "Beam attenuation and chlorophyll concentration as alternative optical indices of phytoplankton biomass," J. Mar. Res. **64,** 431–451 (2006).
44. A. F. Michaels and A. H. Knap, "Overview of the US JGOFS Bermuda Atlantic time-series study and the hydrostation S program," Deep Sea Res., Part II **43,** 157–198 (1996).
45. D. M. Karl and R. Lukas, "The Hawaiian ocean time-series (HOT) program: Background, rationale, and field implementation," Deep Sea Res., Part II **43,** 129–156 (1996).
46. A. Smirnov, B. N. Holben, Y. J. Kaufman, O. Dubovik, T. F. Eck, I. Slutzker, C. Pietras, and R. N. Halthore, "Optical properties of atmospheric aerosol in maritime environments," J. Atmos. Sci. **59,** 501–522 (2002).
47. D. M. Glover, S. C. Doney, A. J. Mariano, R. H. Evans, and S. J. McCue, "Mesoscale variability in time series data: satellite-based estimates for the U.S. JGOFS Bermuda Atlantic time-series study (BATS) site," J. Geophys. Res. **107,** doi:10.1029/2000JC000589 (2002).
48. T. L. Hayward, "The nutrient distribution and primary production in the central North Pacific," Deep-Sea Res. **34,** 1593–1627 (1987).
49. A. F. Michaels, A. H. Knap, R. L. Dow, K. Gunderson, R. J. Johnson, J. Sorensen, A. Close, G. A. Knauer, S. E. Lohrenz, V. A. Asper, M. Tuel, and R. Bidigare, "Seasonal patterns of ocean biogeochemisty at the U.S. JGOFS Bermuda atlantic time-series study site," Deep-Sea Res. Part I **41,** 1013–1038 (1994).
50. N. B. Nelson, D. A. Siegel, and A. F. Michaels, "Seasonal dynamics of colored dissolved material in the Sargasso Sea—implications for biogeochemistry and remote sensing," Deep-Sea. Res. Part I **45,** 931–957 (1998).
51. M. E. Ondrusek, R. R. Bidigare, K. Waters, and D. M. Karl, "A predictive model for estimating rates of primary production in

the subtropical North Pacific Ocean," Deep-Sea Res. Part II **48,** 1837–1864 (2001).
52. C. C. Trees, D. K. Clark, R. R. Bidigare, M. E. Ondrusek, and J. L. Mueller, "Accessory pigments versus chlorophyll a concentrations within the euphotic zone: a ubiquitous relationship," Limnol. Oceanogr. **45,** 1130–1143 (2000).
53. S. B. Hooker, L. Van Heukelem, C. S. Thomas, H. Claustre, J. Ras, R. Barlow, H. Sessions, L. Schlüter, J. Perl, C. Trees, V. Stuart, E. Head, L. Clementson, J. Fishwick, C. Llewellyn, and J. Aiken, *The Second SeaWiFS HPLC Analysis Round Robin Experiment (SeaHARRE-2)* (NASA Goddard Space Flight Center, 2005).
54. H. R. Gordon, "Calibration requirements and methodology for remote sensors viewing the oceans in the visible," Rem. Sens. Environ. **22,** 103–126 (1987).
55. S. W. Brown, B. C. Johnson, M. E. Feinholz, M. A. Yarbrough, S. J. Flora, K. R. Lykke, and D. K. Clark, "Stray-light correction algorithm for spectrographs," Metrologia **40,** S81–S84 (2003).
56. B. A. Franz, P. J. Werdell, G. Meister, S. W. Bailey, R. E. Eplee, Jr., G. C. Feldman, E. Kwiatkowska, C. R. McClain, F. S. Patt, and D. Thomas, "The continuity of ocean color measurements from SeaWiFS to MODIS," Proc. SPIE **5882,** doi:10.1117/12.620069 (2005).
57. D. A. Antoine, J. M. André, and A. Morel, "Oceanic primary production. 2. Estimation at global scale from satellite (CZCS) chlorophyll," Global Biogeochem. Cycles **10,** 57–70 (1996).
58. W. W. Gregg, F. S. Patt, and W. E. Esaias, "Initial analysis of ocean color data from the ocean color and temperature scanner. II. Geometric and radiometric analyses," Appl. Opt. **38,** 5692–5702.
59. W. W. Gregg, M. E. Conkright, J. E. O'Reilly, F. S. Patt, M. H. Wang, J. A. Yoder, and N. W. Casey, "NOAA-NASA coastal zone color scanner reanalysis effort," Appl. Opt. **41,** 1615–1628 (2002).
60. M. Wang, A. Isaacman, B. A. Franz, and C. R. McClain, "Ocean-color optical property data derived from the Japanese ocean color and temperature scanner and the French polarization and directionality of the Earth's reflectances: a comparison study," Appl. Opt. **41,** 974–990 (2002).
61. G. C. Feldman, W. D. Robinson, B. A. Franz, S. W. Bailey, N. Kuring, F. S. Patt, P. J. Werdell, and C. R. McClain, "The coastal zone color scanner," http://oceancolor.gsfc.nasa.gov/CZCS/ (2007).
62. H. R. Gordon, D. K. Clark, J. W. Brown, O. B. Brown, R. H. Evans, and W. W. Broenkow, "Phytoplankton pigment concentrations in the Middle Atlantic Bight: comparison between ship determinations and coastal zone color scanner estimates," Appl. Opt. **22,** 20–36 (1983a).
63. J. L. Mueller, "Nimbus-7 CZCS: Confirmation of its radiometric sensitivity decay rate through 1982," Appl. Opt. **24,** 1043–1047 (1985).
64. B. A. Franz, E. J. Ainsworth, and S. Bailey, "SeaWiFS vicarious calibration: an alternative approach utilizing simultaneous *in situ* observations of oceanic and atmospheric optical properties," in *In Situ Aerosol Optical Thickness Collected by the SIMBIOS Program (1997–2000): Protocols, and Data QC and Analysis,* G. S. Fargion, R. Barnes, and C. McClain, eds. (NASA Goddard Space Flight Center, 2001).
65. J. M. André and A. Morel, "Atmospheric corrections and interpretations of marine radiances in CZCS imagery, revisited," Oceanol. Acta **14,** 3–22 (1991).
66. J. G. Acker, *The Heritage of SeaWiFS: A Retrospective on the CZCS NIMBUS Experiment Team (NET) Program* (NASA Goddard Space Flight Center, 1994).
67. M. Shimada, H. Oaku, Y. Mitomi, H. Murakami, and H. Kawamura, "Calibration of the ocean color and temperature sensor," IEEE Trans. Geosci. Rem. Sens. **37,** 1484–1495 (1999a).
68. G. Zibordi, B. Holben, S. B. Hooker, F. Mélin, J.-F. Berthon, I. Slutzker, D. Giles, D. Vandemark, H. Feng, K. Rutledge, C. Schuster, and A. Al Mandoos, "A network for standardized ocean color validation measurements," EOS Trans. AGU **87,** 293 (2006).
69. E. Bosc, A. Bricaud, and D. Antoine, "Seasonal and interannual variability in algal biomass and primary production in the Mediterranean Sea, as derived from 4 years of SeaWiFS observations," Global Biogeochem. Cycles **18,** doi:10.1029/2003GB002034 (2004).
70. S. W. Brown and B. C. Johnson, "Advances in radiometry for ocean color," Proc. SPIE **5151,** 441–453 (2003).
71. G. Meister, E. J. Kwiatkowska, B. A. Franz, F. S. Patt, G. C. Feldman, and C. R. McClain, "Moderate-Resolution Imaging Spectroradiometer ocean color polarization correction," Appl. Opt. **44,** 5524–5535 (2005).